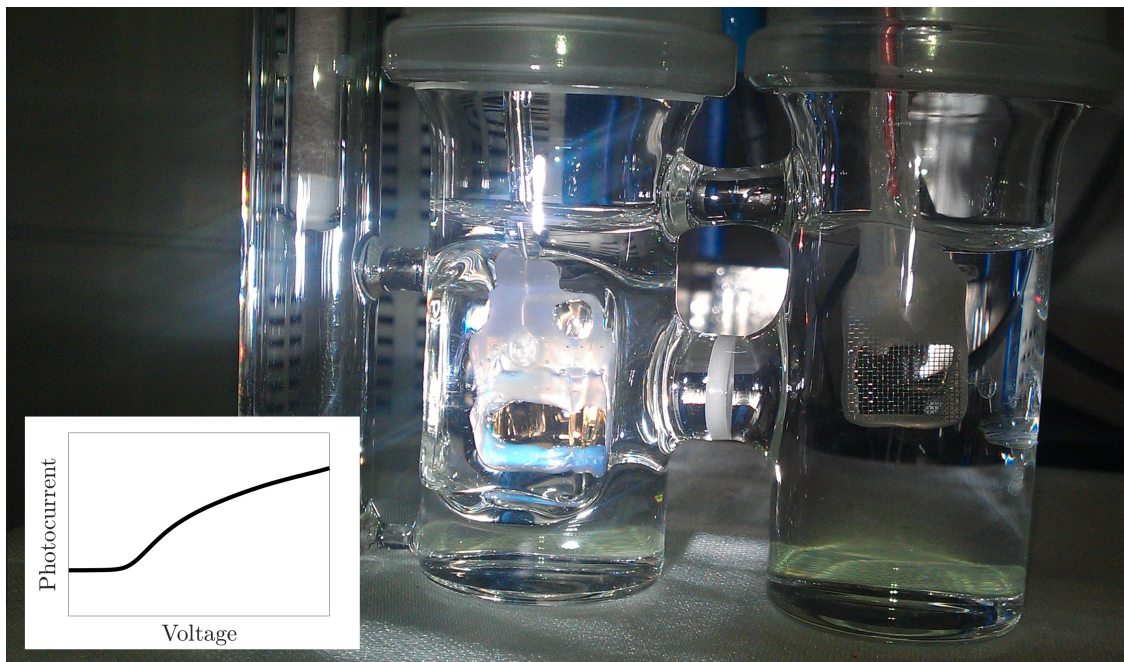




CHALMERS
UNIVERSITY OF TECHNOLOGY



Improving Photoelectrochemical Hydrogen Generation from Water Splitting using Ultrathin Overlayers on Hematite Photo-anodes

Master's thesis in Applied Physics

ALEXANDER LEVINSSON

MASTER'S THESIS 2017

**Improving Photoelectrochemical Hydrogen
Generation from Water Splitting using Ultrathin
Overlayers on Hematite Photo-anodes**

ALEXANDER LEVINSSON



CHALMERS
UNIVERSITY OF TECHNOLOGY

Department of Physics
Division of Chemical Physics
CHALMERS UNIVERSITY OF TECHNOLOGY
Gothenburg, Sweden 2017

Improving Photoelectrochemical Hydrogen Generation from Water Splitting using Ultrathin Overlayers on Hematite Photo-anodes

ALEXANDER LEVINSSON

© ALEXANDER LEVINSSON, 2017.

Supervisor: Aadesh P. Singh, Department of Physics
Examiner: Björn Wickman, Department of Physics

Master's Thesis 2017
Department of Physics
Division of Chemical Physics
Chalmers University of Technology
SE-412 96 Gothenburg
Telephone +46 31 772 1000

Cover: Photo of the PEC cell used during the project. The hematite working electrode is seen in the central compartment, and the platinum counter electrode is located in the right compartment. The graph shows the obtained photocurrent as a function of the applied voltage to the PEC cell.

Typeset in L^AT_EX
Printed by Chalmers Reproservice
Gothenburg, Sweden 2017

Improving Photoelectrochemical Hydrogen Generation from Water Splitting using Ultrathin Overlayers on Hematite Photo-anodes

ALEXANDER LEVINSSON

Department of Physics

Chalmers University of Technology

Abstract

Solar energy is the energy source for the future, because it is renewable and environmentally safe. An application to convert the solar energy into a useful energy form is photoelectrochemical (PEC) water splitting, in which the solar energy is converted to chemical energy in hydrogen gas. Hematite ($\alpha\text{-Fe}_2\text{O}_3$) is one of the most promising semiconductors that are used in PEC cells, mainly because of its band gap of 1.9 – 2.2 eV, its chemical stability, and that it is an abundant material. Hematite is used as a photo-anode in the PEC cell, but its performance is limited due to for instance poor oxidation kinetics at the hematite/electrolyte interface. In this work, three different ultrathin overlayers (FeOOH, NiOOH, NiFeO_x) are deposited on hematite in order to improve the performance of the PEC cell by reducing recombination of photogenerated electron–hole pairs and facilitate hole transport at the hematite/overlayer/electrolyte interface. With these overlayers, the photocurrent density of hematite is increased and the onset potential is lowered. The hematite electrode with the FeOOH overlayer shows the best performance, where the photocurrent density is increased from 0.087 mA/cm² for bare hematite to 0.275 mA/cm² at 1.23 V_{RHE} under 1 sun illumination, and the onset potential is lowered by 220 mV compared to bare hematite. This improved performance is a result of the improved oxidation kinetics, which for instance can be attributed to an increased surface charge transfer efficiency.

Keywords: electrochemistry, hematite, hydrogen, overlayer, photo-anode, photoelectrochemical cell, semiconductor, solar energy, water splitting.

Acknowledgements

First, I would like to thank Björn Wickman for opportunity to do this thesis. Thank you for supporting me throughout the thesis, for your excellent advice, and for allowing me to visit you at your office at any time to discuss and ask questions about the work. I also want to thank Aadesh P. Singh for all your help during the thesis, for your fabrication work in the clean room, for teaching my how to fabricate electrodes in the lab, for the tutorial of the potentiostat, and for answering all my questions. Thanks to the entire group of Chemical Physics for a nice time the past six months, and thanks to Katarina Logg for your time and help with the Raman microscope.

Finally, I want to thank all my friends and my family for supporting me during these five years. Thank you!

Alexander Levinsson, Gothenburg, June 2017

Contents

List of Figures	xi
List of Tables	xv
1 Introduction	1
1.1 Aim of the project	2
1.2 Limitations	3
2 Theoretical Background	5
2.1 Electrochemistry	5
2.1.1 Electrical work	6
2.1.2 Water splitting	7
2.1.3 Reduction and oxidation	8
2.2 Semiconductors	9
2.2.1 Band structure	9
2.2.2 Fermi level and doping	11
2.3 The photoelectrochemical cell	11
2.3.1 Basics of the cell	12
2.3.2 Band bending and flat-band potential	14
3 Hematite	17
3.1 Promising material for PEC cells	17
3.2 Challenges in PEC cells	17
3.3 Modification of hematite electrodes	18
4 Fabrication of hematite photo-anodes	21
4.1 Fabrication of hematite	21
4.2 Deposition of overlayers	22
4.3 Fabrication of electrodes	22
4.3.1 Active surface area	23
5 Experimental Methods	25
5.1 Measurements in the PEC cell	25
5.1.1 Voltammetry	26
5.1.2 Electrochemical Impedance Spectroscopy	27
5.1.3 Mott-Schottky analysis	28
5.1.4 Surface charge separation efficiency	29

5.2	Raman spectroscopy	30
5.3	Light absorption spectroscopy	31
6	Result and discussion	33
6.1	Optimisation of overlayer deposition	33
6.1.1	FeOOH overlayer	33
6.1.2	NiOOH overlayer	35
6.1.3	NiFeO _x overlayer	35
6.2	Comparison between FeOOH, NiOOH, and NiFeO _x overlayers	37
6.2.1	Voltammetry	37
6.2.2	Electrochemical Impedance Spectroscopy	37
6.2.3	Mott-Schottky	39
6.2.4	Surface charge separation	40
6.2.5	Light absorption	42
6.3	Raman spectroscopy	42
7	Conclusion	45
7.1	Outlook	45
	Bibliography	47

List of Figures

2.1	Schematic illustration of the band gap of a semiconductor. The band gap, E_g , is the difference between the conduction band edge and the valence band edge, and no electron energies in the band gap are allowed.	9
2.2	Direct and indirect band gap. Left panel: illustration of a direct band gap transition. There is no change in momentum and the electron is excited from the valence band to the conduction band by absorption of a photon. Right panel: illustration of an indirect band gap transition. The valence band edge and the conduction band edge do not have the same crystal momentum, thus a phonon is needed in the electron excitation process.	10
2.3	The Fermi level of an intrinsic semiconductor is located at the midpoint of the band gap. In this illustration, some electrons are excited to the conduction band, leaving holes in the valence band.	11
2.4	Energy bands and Fermi levels of doped semiconductors. Left panel: In an n-type semiconductor the dopant introduces an energy band, dopant band, close to the conduction band. The electrons in this band are more likely to be excited to the conduction band compared to the electrons in the valence band. This results in more electrons in the conduction band than holes in the valence band, and therefore electrons are the majority charge carriers in an n-type semiconductor. Right panel: In a p-type semiconductor the dopant band is located close to the valence band. The result from this is that electrons in the valence band are easily transferred to the dopant band. This leaves holes in the valence band, hence holes are the majority charge carriers in a p-type semiconductor.	12
2.5	A basic PEC cell with an n-type semiconductor that works as a photo-anode. The photo-anode absorbs incident photons, creating an electron-hole pair. The holes are transferred to the photo-anode/electrolyte interface where they oxidize water, forming oxygen gas and hydrogen ions. The electrons are transferred to the cathode via an external circuit, while the hydrogen ions are transferred to the cathode via the electrolyte. These electrons and hydrogen ions then react at the cathode/electrolyte interface, forming hydrogen gas. A voltmeter can be used to measure the potential between the two electrodes.	13

2.6	Schematic illustration of the energies in an n-type semiconductor under illumination. Note the upward band bending close to the photoanode/electrolyte interface. The applied bias voltage shifts the Fermi level of the cathode to an energy higher than the reduction potential of the electrolyte, which enables water splitting. Without the applied bias voltage, the Fermi level of the cathode may be located below the reduction potential in the electrolyte, thus the electrons have not sufficient energy to produce the hydrogen gas.	15
3.1	The band edge positions for hematite relative vacuum level and normal hydrogen electrode (NHE) in an electrolyte of pH = 7. The reduction and oxidation potentials are also shown.	18
4.1	The sample to the left is coated with a thin 10 nm layer of Fe. The sample to the right is an Fe coated sample after annealing, where the red-orange Fe ₂ O ₃ is obtained.	21
4.2	A schematic side view of the fabricated photo-anode samples. The thermal deposited overlayer is either FeOOH, NiOOH, or NiFeO _x . Note: not drawn to scale.	22
4.3	The electrode to the left is designed with the freehand method, and the electrode to the right is designed with a circular Teflon block to obtain a circular active surface area.	23
5.1	The PEC cell is shown to the left where each electrode is labelled. Note the quartz window that is required in order for the UV radiation to reach the photo-anode. The potentiostat, shown to the right, was used to control the applied bias voltage to the PEC cell during the measurements.	26
5.2	Two circuit models for the PEC cell: Hamann's circuit and Randle's simplified circuit. The two models have the same Fe ₂ O ₃ bulk components and the same ITO/Fe ₂ O ₃ series resistance, but differ in that way that Hamann's circuit includes a surface-state capacitance in parallel with a surface-state resistance.	28
5.3	The energy levels and scattering processes that are included in Raman spectroscopy. Rayleigh scattering is an elastic process that is more common than the other two. However, Stokes and anti-Stokes inelastic scattering includes energy changes in the scattered photon, which in Raman spectroscopy are used to identify the molecules because each molecule has its unique energy states.	30

-
- 6.1 Optimisation of FeOOH overlayer deposition. **Left panel:** optimisation of deposition temperature. The deposition was 5 min for all samples, and 80°C is considered the optimised temperature. **Right panel:** optimisation of deposition time. All overlayers were deposited at 80°C, and the shortest deposition time of 1 min gives the highest current density and lowest onset potential. Dashed lines represent dark currents. Note that these two measurements were performed with electrodes from different Fe depositions in the Lesker evaporator, hence they differ from each other. 34
- 6.2 Optimisation of NiOOH overlayer deposition. **Left panel:** optimisation of deposition temperature. The deposition was 5 min for all samples, and 60°C is considered the optimised temperature, especially due to the lowered onset potential. **Right panel:** optimisation of deposition time. All overlayers were deposited at 60°C, and the deposition time of 5 min gives the lowest onset potential and highest photocurrent density at low applied voltages. Dashed lines represent dark currents. 35
- 6.3 Optimisation of NiFeO_x overlayer deposition. **Left panel:** optimisation of deposition temperature. The deposition was 5 min for all samples, and 90°C is considered the optimised temperature. Note the surprisingly high dark current for the 100°C electrode, and the reason for this is unknown. **Right panel:** optimisation of deposition time. All overlayers were deposited at 90°C, and the shortest deposition time of 1 min shows the best combination of onset potential and current density at low applied bias voltages. Dashed lines represent dark currents. 36
- 6.4 The photocurrent densities for Fe₂O₃ photo-anodes with the three different overlayers FeOOH, NiOOH, and NiFeO_x under 1 sun irradiation. The dashed lines are currents in dark. 38
- 6.5 Nyquist diagrams for EIS measurements under 1 sun irradiation on four different photo-anodes: bare Fe₂O₃, Fe₂O₃-FeOOH, Fe₂O₃-NiOOH, and Fe₂O₃-NiFeO_x. The applied bias voltage is 0.23 V_{Ag/AgCl} ≈ 1.23 V_{RHE}, and the frequency range is 0.1 Hz – 100 kHz. 39
- 6.6 Mott-Schottky measurements in dark for the different photo-anodes bare Fe₂O₃, Fe₂O₃-FeOOH, Fe₂O₃-NiOOH, and Fe₂O₃-NiFeO_x obtained at 1 kHz. Linear plots are extrapolated from the interval 1.0 – 1.2 V_{RHE} and plotted as dotted lines to estimate the flat-band potentials of the different photo-anodes. 40

6.7	Comparison between the current densities obtained in 0.1 M NaOH and 0.1 M NaOH + 0.3 M H ₂ O ₂ electrolyte. Upper left panel: comparison for bare Fe ₂ O ₃ photo-anode. Upper right panel: comparison for Fe ₂ O ₃ -FeOOH photo-anode. Lower left panel: comparison for Fe ₂ O ₃ -NiOOH photo-anode. Lower right panel: comparison for Fe ₂ O ₃ -NiFeO _x photo-anode. Note that the photocurrents obtained in the 0.1 M NaOH electrolyte differ from the ones presented in figure 6.4, which is due to instability issues with the photo-anodes. Dashed lines represent dark currents.	41
6.8	Surface charge transfer efficiency η_{surf} as a function of the applied bias voltage. The surface charge separation efficiency is, especially at low applied bias voltages, increased for the FeOOH and NiFeO _x overlayers. Note that the NiOOH overlayer, unlike to the other two overlayers, does not increase the surface charge separation efficiency significantly.	41
6.9	Absorption spectra as a function of photon energy for the three optimised overlayer photo-anodes and a bare Fe ₂ O ₃ photo-anode. Note the bandgap of Fe ₂ O ₃ that is located around 2 eV.	42
6.10	Raman shifts for a bare Fe ₂ O ₃ photo-anode. Several peaks are observed and they are consistent with reported peaks for Fe ₂ O ₃	43

List of Tables

2.1	Entropies of formation under standard conditions (25°C and 1 atm pressure) of the molecules involved in water splitting [1].	7
6.1	The onset potentials E_{ons} for the electrodes used for optimisation of FeOOH overlayers. The onset potential is here defined as the applied bias voltage where the photocurrent density exceeds 20 $\mu\text{A}/\text{cm}^2$	34
6.2	The onset potentials E_{ons} for the electrodes used for optimisation of NiOOH overlayers. The onset potential is here defined as the applied bias voltage where the photocurrent density exceeds 20 $\mu\text{A}/\text{cm}^2$	36
6.3	The onset potentials E_{ons} for the electrodes used for optimisation of NiFeO _x overlayers. The onset potential is here defined as the applied bias voltage where the photocurrent density exceeds 20 $\mu\text{A}/\text{cm}^2$	37
6.4	The optimised thermal deposition parameters from section 6.1.	37
6.5	Values of resistances and capacitances in Hamann’s circuit obtained by curve fitting of the Nyquist diagrams in figure 6.5.	39
6.6	The estimated flat-band potentials from the Mott-Schottky measurement.	40

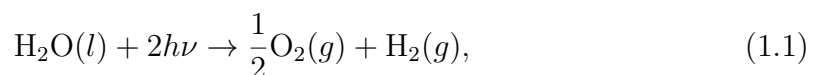
1

Introduction

The modern society we live in consumes more and more energy. This is a result of the increase in Earth's population as well as an increase in the energy consumption per capita [2]. Several of the energy sources that are used today, for instance fossil based fuels and nuclear power, are limited and harmful in a long-term perspective. For a sustainable future for our planet, there is a need for abundant and environmentally safe energy sources that have the potential to supply the high energy demand without being harmful for our planet.

Hydrogen has a promising future as an energy carrier and as a fuel [3]. In nature, hydrogen is only found in chemical compounds, therefore the use of hydrogen as energy carrier or fuel first requires energy to generate hydrogen gas. Hydrogen as a fuel can be compared with fossil based fuels, which are mainly used today, in terms of a sustainable future. As already mentioned, fossil based fuels are a limited source and have a negative impact on the environment. Hydrogen on the other hand is abundant in compound form, for instance in water, and it can be used as an environmentally friendly fuel, especially when generated from a renewable energy source. The only renewable energy source that has the potential to supply all the energy that we consume is the sun. The estimated average energy consumption for our planet in 2015 was 14.5 TW [4], which can be compared to the solar power that irradiates the surface of the Earth: $1.3 \cdot 10^5$ TW [5]. This means that the energy from one hour of solar illumination equals Earth's total energy consumption in one year.

The solar cells, where the solar energy is converted directly into electricity, has been improved a lot the last decades. However, an issue with solar cells is the intermittency problem; the electricity is not produced when and where it is needed at most. An alternative to solar cells is photoelectrochemical (PEC) cells. In a PEC cell, the solar energy is converted to storable chemical energy, which has the potential to solve the intermittency problem. The solar energy can be used to generate hydrogen gas, which can be used as a fuel or an energy carrier. Hydrogen can be generated from water splitting, with the overall reaction



where $h\nu$ is the energy of the incident photon [6]. The threshold energy for the reaction to occur is 1.23 eV [3].

PEC water splitting with solar energy is a complex process, which will be explained and discussed throughout this thesis. One essential part of the process is absorption of the solar energy. For this, a semiconducting material is used. The

bandgap of the semiconductor gives the theoretical maximum driving force for water splitting. In science, several different semiconductors have been used for PEC water splitting, and especially metal oxides have been widely used. Some examples of material used are α -Fe₂O₃, BiVO₄, CdS, Cu₂O, GaP, TiO₂, WO₃, and ZnO [7].

PEC cells have existed in 45 years. The first demonstration of a PEC water splitting system to produce hydrogen gas was given by Fujishima and Honda in 1972, where they used the semiconductor TiO₂ [6]. In 1998, the high potential for PEC water splitting was demonstrated by Khaselev and Turner when they achieved a solar-to-hydrogen (STH) conversion efficiency of 12.4% [8], which is higher than the benchmark STH efficiency of 10% for practical applications [7]. The STH conversion efficiency measures the overall performance of a PEC cell, and describes how much of the solar energy that is converted into chemical energy in hydrogen gas. Research is ongoing to increase the performance of PEC cells. More advanced PEC systems are developed to increase the STH conversion efficiency and the highest reported STH efficiency today is over 30% [9].

In this study, the material α -Fe₂O₃, which is named hematite, is used. Hematite has been widely used and analysed in PEC water splitting both because of its stability and suitable bandgap. Today, research is ongoing to increase the understanding and the performance of PEC cells using hematite as light absorbing semiconductor. To increase the performance of hematite in a PEC cell one can modify the material. Examples of modifications of hematite are depositing a thin overlayer of an oxide-hydroxide [10], doping the hematite, for instance with titanium [11], and treat the material with hydrogen gas during the annealing process, in which the hematite is generated [12].

1.1 Aim of the project

The aim of this project is both to optimise the performance and increase the understanding of a PEC system comprising a uniform hematite photo-anode and a thin overlayer of FeOOH, NiOOH, or NiFeO_x. To achieve the aim, the following questions will be answered:

- How does an overlayer affect the properties and performance of a hematite photo-anode?
- Why does an overlayer affect the performance of a hematite photo-anode?
- What conditions for each overlayer deposition gives the best performance of the PEC cell?
- Which overlayer gives the best performance of the PEC cell? Why?

The understanding of the PEC system is of great importance in the project. Therefore, the aim is not only to explain why some experiments show good results, but also to understand why some experiments do not work as intended.

1.2 Limitations

One important limitation is that the same basic PEC cell is used in all measurements. The system consists of hematite as photo-anode, platinum as cathode, and aqueous NaOH as electrolyte. All tests are done at room temperature and under 1 atm pressure. Regarding the overlayers, a limitation is set to include the three overlayers FeOOH, NiOOH, and NiFeO_x. Finally, the amount of theory will be at a level of detail that is relevant to the scope and aim of the project.

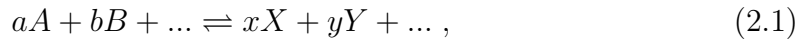
2

Theoretical Background

This chapter intends to give a theoretical background of the most important concepts in this thesis. The experimental work is based on these concepts, but this background is given for a general water splitting photoelectrochemical cell.

2.1 Electrochemistry

Knowledge about electrochemistry is of great importance to understand the chemical reactions that occur in a photoelectrochemical cell. A general chemical reaction can be written



where A, B, \dots are the reactants and X, Y, \dots are the products. Both the reactants and the products can be in any physical state: solid, liquid, or gaseous. To study the direction of the reaction (2.1), thermodynamics, and especially Gibbs free energy, is used. Gibbs free energy is defined as

$$G(p, T) = U + pV - TS = H - TS , \quad (2.2)$$

where U is the internal energy of the system, p is the pressure, V is the volume, T is the temperature, S is the entropy, and H is the enthalpy [1]. At constant pressure and temperature, a change in Gibbs free energy is

$$\Delta G = \Delta U + p\Delta V - T\Delta S = \Delta H - T\Delta S . \quad (2.3)$$

Gibbs free energy can be related to the second law of thermodynamics, which states that the total entropy only can increase with time or remain constant, that is $\Delta S_{\text{tot}} \geq 0$. The differential of Gibbs free energy at constant pressure and temperature is

$$dG = dU + p dV - T dS . \quad (2.4)$$

The total entropy can be written

$$S_{\text{tot}} = S + S_R , \quad (2.5)$$

where S is the entropy of a given system and S_R is the entropy of a large reservoir [1]. The fundamental thermodynamic relation is

$$dU = T dS - p dV , \quad (2.6)$$

which can be written as

$$dS = \frac{1}{T} dU + \frac{p}{T} dV. \quad (2.7)$$

Consider a small change in entropy:

$$dS_{\text{tot}} = dS + dS_R, \quad (2.8)$$

and applying equation (2.7) to the entropy of the reservoir gives

$$dS_{\text{tot}} = dS + \frac{1}{T_R} dU_R + \frac{p_R}{T_R} dV_R. \quad (2.9)$$

The temperature and pressure are the same in the system and reservoir, and since the change in energy and volume of the reservoir is minus the change in energy and volume of the system, respectively, equation (2.9) gives

$$dS_{\text{tot}} = dS - \frac{1}{T} dU - \frac{p}{T} dV = -\frac{1}{T} (dU + p dV - T dS) = -\frac{1}{T} dG. \quad (2.10)$$

Therefore, changes in Gibbs free energy is related to entropy changes via

$$\Delta G = -T \Delta S_{\text{tot}}, \quad (2.11)$$

and an increase in entropy always corresponds to a decrease in Gibbs free energy. Note the difference between equation (2.3) and (2.11). Equation (2.11) includes both the given system and a reservoir, which has $\Delta H_{\text{tot}} = \Delta H + \Delta H_R = 0$ under the given conditions. Therefore, $\Delta G \leq 0$ is a condition for a chemical reaction to occur spontaneously.

2.1.1 Electrical work

Consider a system that contains two different conducting objects. If these objects are brought into contact, an electric potential difference is developed at the interface. The electrical potential difference is developed because of charge separation that occurs between the two objects [13].

Electrical work is done when an electric charge is moved through an electric potential difference. This electrical work can be related to a change in Gibbs free energy. The first law of thermodynamics is stated

$$\Delta U = q + w, \quad (2.12)$$

where q is the heat absorbed by the system and w is the work done on the system. In the case of both mechanical and electrical work under constant pressure, the work done on the system is [13]

$$w = w_{\text{mech}} + w_{\text{elec}} = -p\Delta V + w_{\text{elec}}. \quad (2.13)$$

For a reversible process under constant temperature, the heat absorbed by the system is given by

$$q = T\Delta S. \quad (2.14)$$

Combining the equations (2.13) and (2.14) with equation (2.12) gives

$$\Delta U = T\Delta S - p\Delta V + w_{\text{elec}}, \quad (2.15)$$

which also can be written

$$w_{\text{elec}} = \Delta U + p\Delta V - T\Delta S \stackrel{\text{eq(2.3)}}{=} \Delta G. \quad (2.16)$$

The electrical work that is done by the system on the surroundings is

$$w_{\text{elec}} = -EQ, \quad (2.17)$$

where E is the potential difference and Q is the charge that is moved through the potential difference [13]. If the charge carriers are electrons, the electrical work is

$$w_{\text{elec}} = -nFE, \quad (2.18)$$

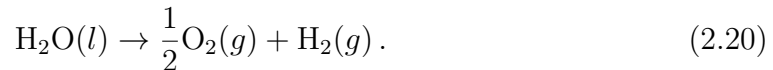
where n is the number of moles of electrons and $F = 96\,484.6$ C [14] is the charge of one mole of electrons, called the Faraday constant. Using equation (2.16), the change in Gibbs free energy can be written

$$\Delta G = -nFE. \quad (2.19)$$

This gives a method to determine changes in Gibbs free energy without having to include calculations of enthalpies and entropies.

2.1.2 Water splitting

The most essential chemical reaction in this thesis is water splitting, which can be written



Consider the reaction for one mole of water, in which one mole of hydrogen gas and half a mole of oxygen gas is generated. The enthalpy change at room temperature and 1 atm pressure for this reaction is $\Delta H = 286$ kJ [1], which means that this amount of energy needs to be added to the system in order for the reaction to occur. As can be seen in equation (2.3), $\Delta H = \Delta U + p\Delta V$. When splitting one mole of water, the generated gases have a larger volume than the water, and the energy that is needed to push the atmosphere away and make space for these gases is $p\Delta V = 4$ kJ [1]. The remaining 282 kJ is the internal energy change in the system.

The amount of electrical work that needs to be done on the system can be calculated. First, the entropy change in the system is analysed. The entropies for each molecule is shown in table 2.1. The entropy change is given by

Table 2.1: Entropies of formation under standard conditions (25°C and 1 atm pressure) of the molecules involved in water splitting [1].

Molecule	Entropy [$\text{JK}^{-1}\text{mol}^{-1}$]
H_2O	69.91
H_2	130.68
O_2	205.14

$$\Delta S = S_{\text{H}_2} + \frac{1}{2}S_{\text{O}_2} - S_{\text{H}_2\text{O}} = 130.68 \text{ J/K} + \frac{205.14}{2} \text{ J/K} - 69.91 \text{ J/K} = 163.34 \text{ J/K},$$

which in turn gives the heat absorbed by the system at room temperature

$$q = 298 \text{ K} \cdot 163.34 \text{ J/K} \approx 49 \text{ kJ}.$$

The change in Gibbs free energy, which is equal to the electrical work done on the system, is according to equation (2.3)

$$\Delta G = 286 \text{ kJ} - 49 \text{ kJ} = 237 \text{ kJ}.$$

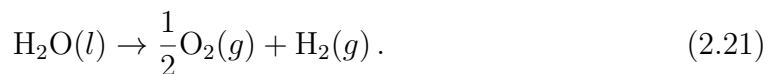
This means that in order to split one mole of water, a minimum of 237 kJ of electrical work is required to enter the system. This can be converted to the amount of electrical work that is required to split one single water molecule:

$$\Delta G = \frac{237 \cdot 10^3}{N_{\text{A}}} \text{ J} \approx \frac{237 \cdot 10^3}{N_{\text{A}}} \cdot 6.242 \cdot 10^{18} \text{ eV} \approx 2.46 \text{ eV},$$

where $N_{\text{A}} \approx 6.022 \cdot 10^{23} \text{ mol}^{-1}$ is the Avogadro constant. This means that a minimum of 2.46 eV of electrical work is required to split one water molecule according to the reaction in equation (2.20).

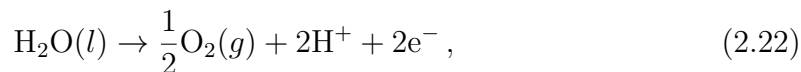
2.1.3 Reduction and oxidation

Two important concepts in this thesis are reduction and oxidation. Reduction is the gain of one or several electrons by an atom, molecule, or ion. Oxidation is the loss of one or several electrons from an atom, molecule, or ion. Oxidation and reduction occur simultaneously, and the phenomenon is called a redox reaction. An example of a redox reaction is water splitting:



In the reaction, oxygen is oxidised from its oxidation number -2 in water to the oxidation number 0 in O_2 . At the same time, hydrogen is reduced from its oxidation number $+1$ in water to oxidation number 0 in H_2 .

In electrochemistry, the water splitting is divided into two steps. Oxidation takes place according to the reaction



and reduction takes place according to the reaction



2.2 Semiconductors

Semiconductors are materials that are characterised by a lower conductivity than metals and higher conductivity than insulators at standard temperatures. Most of the semiconductors are solid binary compounds with a crystalline structure. Semiconductors are used in a lot of applications; apart from photoelectrochemical cells they are also used in photovoltaic cells, transistors, diodes, detectors, etcetera [15].

2.2.1 Band structure

The band structure describes the energies that an electron in a material can have. The energy bands are made up of atomic orbitals from individual atoms, and due to the large number of atoms in the material, the difference between adjacent energies in an energy band is so small that an energy band can be seen as a continuum of energies. Two energy bands are of interest, the highest occupied band called the valence band, and the lowest unoccupied band called the conduction band. The highest energy in the valence band is called the valence band edge and the lowest energy in the conduction band is called the conduction band edge. The difference between these energies is called the band gap, E_g , and it determines the most essential properties of the semiconductor [16]. The electron energies between the valence band and conduction band are forbidden, which means that no electrons are allowed to have these energies. The band gap is illustrated in figure 2.1.

Electrons can be excited from the valence band to the conduction band thermally or photochemically [16], and the number of electrons that are thermally excited increases with the temperature [15]. When an electron is excited to the conduction band, a positively charged electron hole is left behind in the valence band. This lack of an electron is called a hole and is denoted h^+ . Holes are considered mobile in the way that they change location when an electron is transferred to the vacancy, for example if an electron is transferred from location A to B, a hole is transferred from location B to A simultaneously.

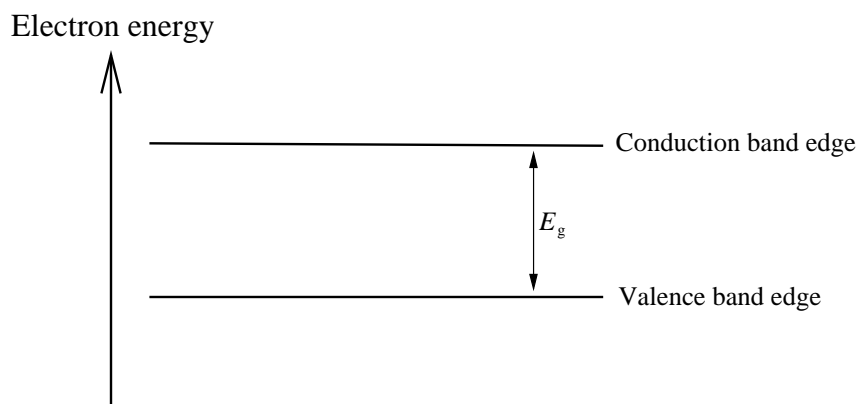


Figure 2.1: Schematic illustration of the band gap of a semiconductor. The band gap, E_g , is the difference between the conduction band edge and the valence band edge, and no electron energies in the band gap are allowed.

2. Theoretical Background

There are two different types of band gaps: direct band gap and indirect band gap. The valence band edge and conduction band edge have a certain crystal momentum, which is a conserved quantity associated with a wave vector [15]. The band gap is direct if the valence band edge and the conduction band edge have the same wave vector, which is illustrated in the left panel of figure 2.2. The absorbed photon has a negligible wave vector, thus there is no change in the crystal momentum for a direct optical transition. Instead, if the valence band edge and the conduction band edge have different wave vectors, the band gap is indirect. This situation is illustrated in the right panel of figure 2.2, and to conserve the crystal momentum of the system the transition involves both a photon and a phonon. The phonon energy is very small compared to the size of a typical band gap, which means that the transition can be described as a two-step process. First the photon energy is absorbed to an intermediate state, in which the crystal momentum has not changed. The second step involves the phonon, which changes the momentum of the electron. If the phonon needed for the transition already exists in the crystal, i.e. is thermally excited, it can be absorbed in the transition. If the phonon is not thermally excited, it can instead be created in the photon absorption process. In this case, the phonon created has the opposite momentum of the electron momentum change, since the quantity is conserved [15]. However, since an indirect band gap transition requires interaction with a phonon, it has a lower probability to occur compared to a direct band gap transition. This results in a lower light absorption coefficient for an indirect band gap, which is a disadvantage for semiconductors that are used in for instance solar cells and PEC cells.

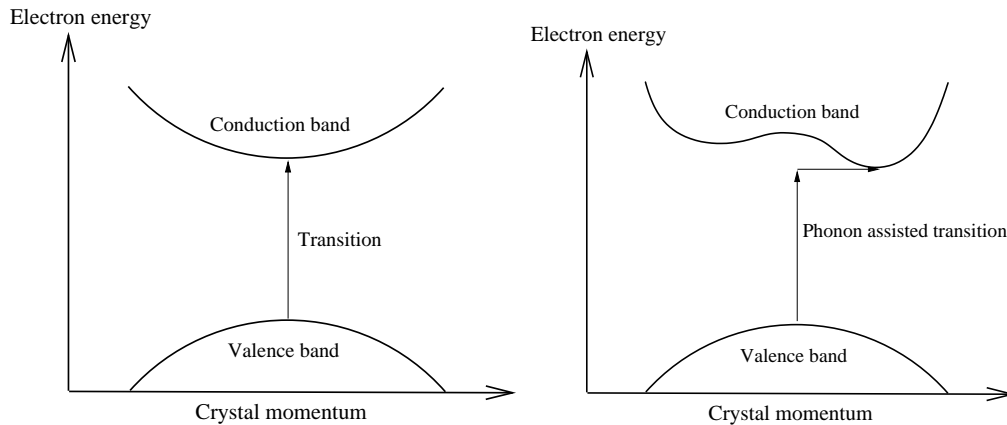


Figure 2.2: Direct and indirect band gap. **Left panel:** illustration of a direct band gap transition. There is no change in momentum and the electron is excited from the valence band to the conduction band by absorption of a photon. **Right panel:** illustration of an indirect band gap transition. The valence band edge and the conduction band edge do not have the same crystal momentum, thus a phonon is needed in the electron excitation process.

2.2.2 Fermi level and doping

The Fermi level of a material is defined as the energy which has the probability $\frac{1}{2}$ to be occupied by an electron. For an undoped, also called intrinsic, semiconductor the Fermi level is located at the mid-point of the band gap [16], which is shown in figure 2.3.

Semiconductors can also be doped by adding a fraction of some dopant element. The most common effect from a dopant is that it introduces a new energy level in the former forbidden band gap area, which changes the charge carrier concentrations and the Fermi level of the material [16]. If the new energy level is located close to the conduction band edge it will facilitate transfer of electrons to the conduction band, and the electrons are the majority charge carriers of the material [16]. The Fermi level is located between the new energy level and the conduction band, and this is called an n-type semiconductor. The left panel of figure 2.4 shows the energy bands and the Fermi level of an n-type semiconductor.

If the majority charge carriers are holes, the semiconductor is a p-type. The new energy level caused by the dopant is located close to the valence band, which facilitates transfer of electrons from the valence band to the new energy level [16]. This results in fewer electrons in the conduction band, and more holes in the valence band. The Fermi level is located just above the valence band, which is illustrated in the right panel of figure 2.4.

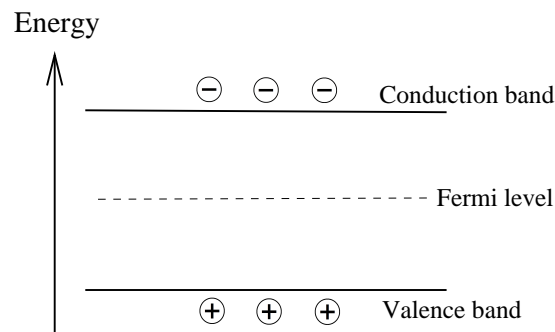


Figure 2.3: The Fermi level of an intrinsic semiconductor is located at the mid-point of the band gap. In this illustration, some electrons are excited to the conduction band, leaving holes in the valence band.

2.3 The photoelectrochemical cell

The main principle of a PEC cell is to, via water splitting, convert solar energy to hydrogen gas, in which the energy is stored in chemical bonds. The solar energy is first absorbed by a semiconductor, and then the holes and electrons are separated from each other and take part in the oxidation and reduction reactions, respectively, to generate the hydrogen gas.

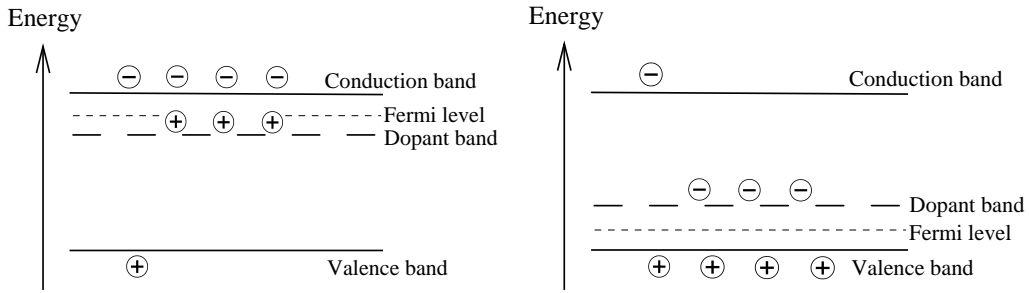
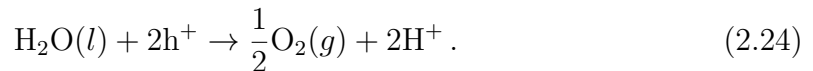


Figure 2.4: Energy bands and Fermi levels of doped semiconductors. **Left panel:** In an n-type semiconductor the dopant introduces an energy band, dopant band, close to the conduction band. The electrons in this band are more likely to be excited to the conduction band compared to the electrons in the valence band. This results in more electrons in the conduction band than holes in the valence band, and therefore electrons are the majority charge carriers in an n-type semiconductor. **Right panel:** In a p-type semiconductor the dopant band is located close to the valence band. The result from this is that electrons in the valence band are easily transferred to the dopant band. This leaves holes in the valence band, hence holes are the majority charge carriers in a p-type semiconductor.

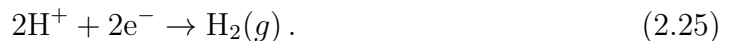
2.3.1 Basics of the cell

A PEC cell consists of three main parts: a working electrode, a counter electrode, and an aqueous electrolyte. The working electrode is a semiconductor with the ability to absorb photons, while the counter electrode often is a metal, for instance platinum is widely used [3]. The purpose of the electrolyte is both to supply the system with water and to transfer charges between the two electrodes.

As mentioned in section 2.1.3, the water splitting is divided into two steps. One reaction step occurs at the working electrode, and the other step at the counter electrode. The electrode where the oxidation occurs is called the anode, and where the reduction occurs is called cathode. For an n-type semiconductor, the electrode is a photo-anode. First, the semiconductor is illuminated with sunlight, and photons with a higher energy than the band gap can be absorbed, creating an electron-hole pair. The excited electrons in the conduction band are then separated from the holes: the electrons are transferred to the cathode via an external circuit, and the holes are transferred to the photo-anode/electrolyte interface [3]. The holes take part in the oxidation that occurs at the photo-anode/electrolyte interface, according to



The oxidation generates both oxygen gas and hydrogen ions at the photo-anode. The hydrogen ions move through the electrolyte to the cathode, where they take part in the reduction process at the cathode/electrolyte interface, together with the electrons from the external circuit. This generates hydrogen gas, according to the reaction



In the case of a p-type semiconductor, the semiconductor instead acts as a photo-

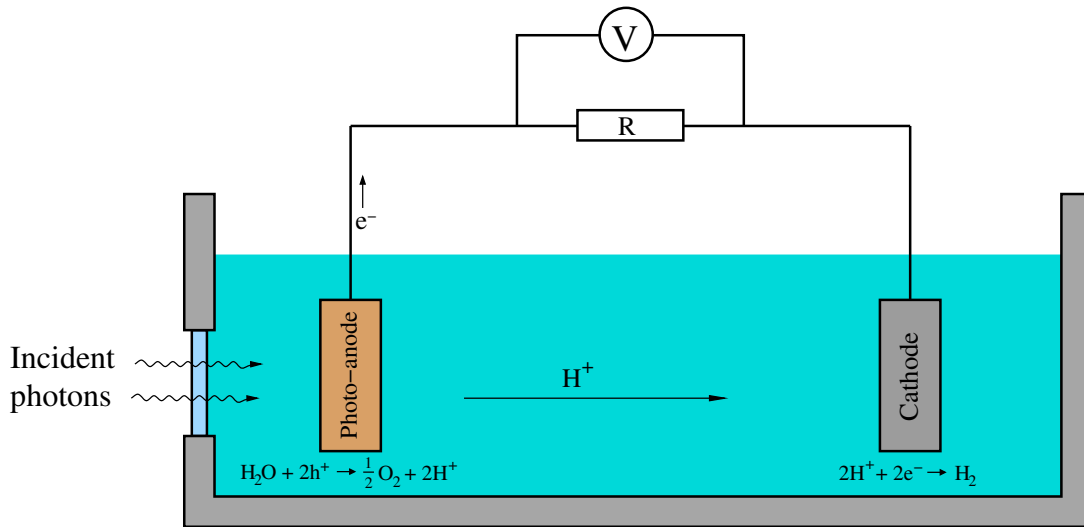
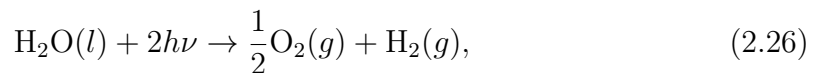


Figure 2.5: A basic PEC cell with an n-type semiconductor that works as a photo-anode. The photo-anode absorbs incident photons, creating an electron-hole pair. The holes are transferred to the photo-anode/electrolyte interface where they oxidize water, forming oxygen gas and hydrogen ions. The electrons are transferred to the cathode via an external circuit, while the hydrogen ions are transferred to the cathode via the electrolyte. These electrons and hydrogen ions then react at the cathode/electrolyte interface, forming hydrogen gas. A voltmeter can be used to measure the potential between the two electrodes.

cathode, which means that reduction takes place at the working electrode. However, the overall reaction in a PEC cell is independent of the type of the semiconductor. The overall reaction is



where $h\nu$ is the photon energy [6]. In order to split one water molecule, there is a need of two photons, which also can be seen in equation (2.24) because two holes are required for the oxidation. As calculated in section 2.1.2, electrical work of 2.46 eV is required to split one water molecule. This means that the threshold photon energy and band gap size is 1.23 eV; it is not theoretically possible to split water in a PEC cell using a semiconductor with a band gap smaller than 1.23 eV. Figure 2.5 illustrates how a basic PEC cell works.

Nevertheless, there is often a need to apply an external bias voltage to the system in order to achieve water splitting. This is due to the positions of the electron bands in the working electrode and the Fermi level of the counter electrode, with respect to the redox potentials in water splitting. The holes of interest are located in the valence band, and because they have a positive charge, the valence band edge must be located at a lower energy than the $\text{H}_2\text{O}/\text{O}_2$ oxidation potential in order for the oxidation to occur spontaneously [17]. The situation is similar for the electrons. The electrons in the conduction band are transferred to the metal counter electrode. The Fermi level of this electrode must have a higher energy than the H^+/H_2 potential in order for the reduction to occur spontaneously [17]. This means that not only the

size of the band gap, but also the position of the band edges and the Fermi level, are important to achieve water splitting.

There is also a lot of losses in a PEC cell. An example is recombination of an excited electron-hole pair, which means that the excited electron loses its absorbed energy as heat and is transferred back to the valence band again. Other typical losses are due to resistance of both electrodes and electrical connections, and voltage losses at the contacts in the cell. All combined losses are estimated to approximately 0.8 eV. In practice, the optimal band gap size is therefore about 2 eV instead of the theoretical limit of 1.23 eV [3].

For a semiconductor to be suitable for applications in a PEC cell, several criteria must be met. As mentioned above, the band gap should not be smaller than about 2 eV. On the other hand, if the band gap is too large, for instance 3 eV or above, only a small fraction of the photons in the solar spectrum can be absorbed, resulting in a too low efficiency of the PEC cell. The energies of the valence band, conduction band, and the Fermi level are also of great importance. For long term use, the semiconductor should not be susceptible for corrosion in the electrolyte, while for large scale applications it should neither be made of rare or expensive elements. It is indeed a challenge to find a semiconductor that fulfils all these criteria.

In science, a third electrode is often used in a PEC cell. This electrode is a reference electrode, and the advantage of using a reference electrode is that the measured potential difference between the working electrode and the reference does not depend on the amount of current in the PEC cell. The stable potential of the reference enables studies of the working electrode. This would not be possible without the reference, since the potential difference between the working electrode and the counter electrode depends, in an unknown way, on the amount of current in the cell [18].

2.3.2 Band bending and flat-band potential

Up to this point, the energy levels have been analysed individually for the electrodes in the PEC cell. However, the electrodes are in contact with the electrolyte, and the system strives towards equilibrium. To be in equilibrium, the electrochemical potentials of the components in the cell must be the same.

Consider the semiconductor/electrolyte interface. The potential of the electrolyte is determined by its redox potential, and the potential of the semiconductor is determined by its Fermi level [16]. If their initial potentials are not the same, charges will move between the semiconductor and the electrolyte in order to achieve equilibrium. These excess charges in a semiconductor are located about 10 – 1 000 nm into the material in a region called the space charge region [16]. The charges in the space charge region generates an electric field, which can be used to separate holes from electrons. For an n-type semiconductor, the Fermi level is higher than the redox potential of the electrolyte, hence electrons are transferred from the semiconductor to the electrolyte in order to achieve equilibrium. This results in a positive charged semiconductor close to the electrolyte interface, which in turn results in an upward bending of the electron bands. This space charge region is also called depletion layer, because the majority charge carriers have been removed from it. Figure 2.6

shows an example of the energies and the band bending in a PEC cell with an n-type semiconductor under illumination and with an applied bias voltage.

The situation is opposite for a p-type semiconductor. Holes are transferred from the semiconductor to the electrolyte, resulting in a downward band bending. Anyway, the space charge region is also a depletion layer since the majority charge carriers in a p-type semiconductor are holes.

The Fermi level and the band edges in the semiconductor can be shifted by applying an external bias voltage to the PEC cell. However, the energies at the semiconductor/electrolyte interface do not change when an external potential is applied, thus the applied potential change both the direction and the magnitude of the band bending. The applied potential at which the Fermi level of the semiconductor is the same as the electrolyte redox potential is called the flat-band potential, E_{fb} [16]. At this applied potential, there is no charge transfer between the semiconductor and the electrolyte, hence no band bending. Note that no current will flow in the PEC cell at the flat-band potential because there is no electric field that can separate holes and electrons [16]. For an n-type semiconductor at potentials negative to E_{fb} , there is an excess of electrons, resulting in an accumulation region. For a p-type semiconductor the accumulation region arises for potentials above E_{fb} .

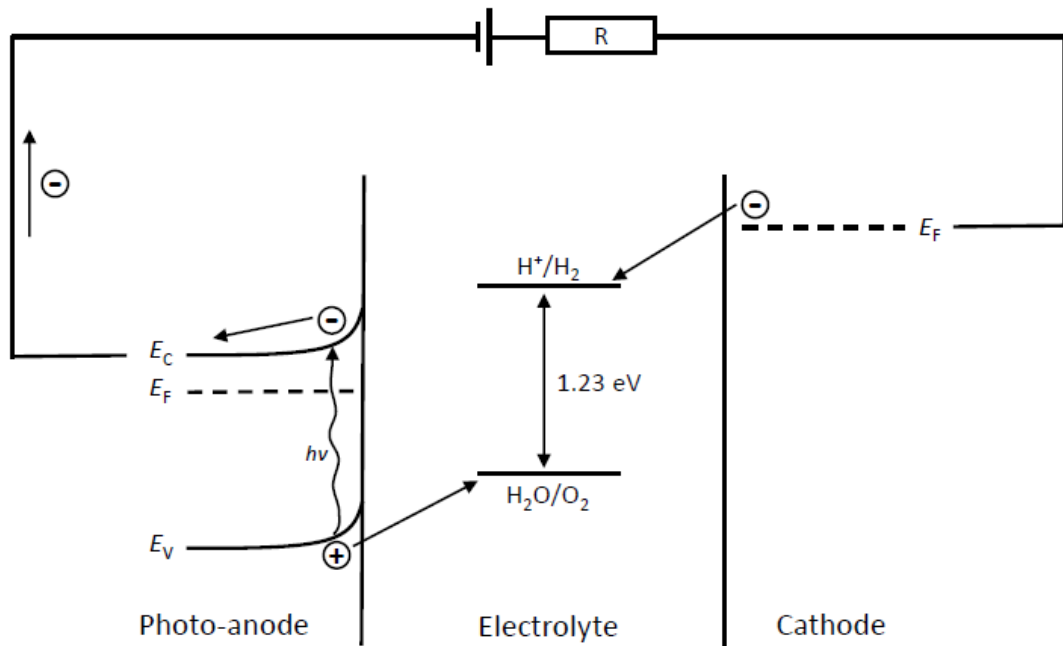


Figure 2.6: Schematic illustration of the energies in an n-type semiconductor under illumination. Note the upward band bending close to the photo-anode/electrolyte interface. The applied bias voltage shifts the Fermi level of the cathode to an energy higher than the reduction potential of the electrolyte, which enables water splitting. Without the applied bias voltage, the Fermi level of the cathode may be located below the reduction potential in the electrolyte, thus the electrons have not sufficient energy to produce the hydrogen gas.

2. Theoretical Background

3

Hematite

The semiconductor that is solely studied in this project is hematite. Hematite is an iron oxide with the chemical formula α -Fe₂O₃, henceforward abbreviated Fe₂O₃. Fe₂O₃ shows an n-type behaviour, and can therefore act as a photo-anode in a PEC cell.

3.1 Promising material for PEC cells

Fe₂O₃ has several material properties that makes it suitable for PEC cells. It has an indirect band gap of 1.9 – 2.2 eV, which corresponds to a theoretical maximum solar-to-hydrogen efficiency of 15%. This can be compared with the benchmark efficiency of 10% [7]. The band energies for Fe₂O₃ are shown, together with the redox potentials for water splitting, in figure 3.1. In addition to an almost optimal band gap size, Fe₂O₃ is inexpensive and the most common iron oxide in nature, hence it has potential for large scale applications [19]. Fe₂O₃ is also the most thermodynamically stable form of iron oxides under relevant conditions for PEC cells [7]. The combination of these properties makes it one of the most interesting materials for PEC cells.

3.2 Challenges in PEC cells

Fe₂O₃ also has some drawbacks for PEC cells. As can be seen in figure 3.1, the conduction band edge has a lower energy than the H⁺/H₂ potential, thus an applied bias voltage is required in order to generate hydrogen gas in the cell. The valence band edge is located at a lower energy than the H₂O/O₂ potential, which means that the oxidation can occur spontaneously. However, the holes in the valence band has a large overpotential, resulting in poor oxidation reaction kinetics. The large overpotential requires a large applied bias voltage to oxidize water, and it is considered a major challenge to reduce the applied bias voltage. The water oxidation kinetics is determined by three processes: absorption of photons to create an electron-hole pair, charge separation efficiency where the holes are transferred to the hematite/electrolyte interface and the electrons to the external circuit, and charge injection efficiency where the holes are collected at the hematite/electrolyte interface to take part in the oxidation reaction [7].

Fe₂O₃ also has poor light absorption because of the indirect band gap. When a photon is absorbed, the excited-state lifetime is very short, in the range of a few picoseconds. Besides that, the electrical conductivity is poor and the diffusion

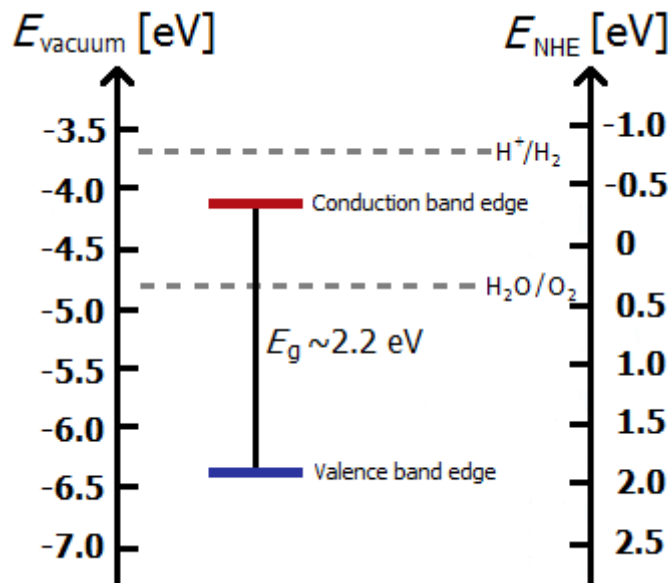


Figure 3.1: The band edge positions for hematite relative vacuum level and normal hydrogen electrode (NHE) in an electrolyte of $\text{pH} = 7$. The reduction and oxidation potentials are also shown.

length of the holes is very short, approximately 2–4 nm. The thickness of the Fe_2O_3 photo-anode can be increased to absorb more photons, but due to the short hole diffusion length only the holes generated in the vicinity of the Fe_2O_3 /electrolyte interface can diffuse to the interface and be used for water oxidation. The other holes, generated further away from the interface, will recombine with electrons and the absorbed energy is lost as heat [7].

3.3 Modification of hematite electrodes

A uniform thin film of Fe_2O_3 as photo-anode results in a too low efficiency for the PEC cell due to the short diffusion length of holes. To increase the Fe_2O_3 /electrolyte interface area, several different nanostructures of Fe_2O_3 have been studied. Some examples of these nanostructures are nanoparticles [20], nanorods [21], nanotubes [22], and nanocones [23].

Two other ways to improve the performance of Fe_2O_3 in a PEC cell is to add a co-catalyst or a surface passivation layer between the Fe_2O_3 and the electrolyte. Two effects can be achieved with this: increase of the generated photocurrent in the cell, and decrease of the onset potential. The latter is the applied bias voltage at which the water splitting begins and a photocurrent is observed. A decrease of the onset potential corresponds to lowering the overpotential of the water oxidation [7].

What a co-catalysts does is to facilitate water oxidation by first oxidize a metal part of itself, thereby facilitate transport of holes from the Fe_2O_3 surface to the electrolyte. Examples of two abundant metals that co-catalysts have been based on are cobalt and nickel. Nickel is considered one of the most interesting co-catalysts since it has shown an efficient performance, is inexpensive, and has a low toxicity

[7]. Nickel oxyhydroxide, NiOOH, is one example of a co-catalyst that has been reported to lower the onset potential [24].

In order to understand the role of a surface passivation layer, the hole transfer from Fe_2O_3 to the electrolyte must be analysed. Holes that have been transferred to the Fe_2O_3 /electrolyte interface still have a non-negligible risk to recombine with an excited electron. The transfer of holes that leads to the water oxidation occurs mostly from surface trapped holes, instead of holes directly from the valence band. The effect from this is that the photocurrent is noticeable only after these surface trapped sites have been accumulated with holes [25]. If these surface states are directly involved in the water oxidation or only act as traps that cause harmful recombination of holes and electrons are still under debate [7]. However, what a surface passivation layer does is to reduce these surface defects, which in turn reduces the recombination rate of holes at the interface [26]. Two examples of passivation layers that have been studied are iron oxyhydroxide, FeOOH [10, 11], and nickel iron oxide, NiFeO_x [27].

3. Hematite

4

Fabrication of hematite photo-anodes

This chapter includes the whole fabrication process of the photo-anodes fabricated during this project: fabrication of pure hematite, deposition of co-catalyst and passivation overlayers, and fabrication of the electrodes used in the PEC cell.

4.1 Fabrication of hematite

Hematite were fabricated on indium tin oxide (ITO), which is a transparent conducting oxide, coated glass pieces of size $10\text{ mm} \times 15\text{ mm}$. A silicon dioxide (SiO_2) layer is located between the glass and ITO and functions as an adhesive layer for the ITO. The samples were first cleaned with oxygen plasma for two minutes, before about 75% of the ITO sides were coated with a 10 nm thin layer of Fe. The Fe deposition took place in a Lesker evaporator and at a pressure below $5 \cdot 10^{-7}$ mbar. The coating technique is called electron beam physical vapor deposition (EBPVD). An iron target is bombarded with an electron beam, which heats the material and evaporates Fe atoms into a gas phase. These atoms are then transformed back into a solid state, and some are transformed just at the ITO substrate, which results in the desired Fe coating.

The Fe coated ITO glass samples were annealed in a furnace to obtain a red-orange thin Fe_2O_3 film. First, the samples were placed in the centre of the furnace, which was then heated up to 500°C during two hours. The annealing then continued at 500°C for eight hours, followed by a naturally cool down to room temperature. Figure 4.1 shows two Fe coated sample, one before and one after the annealing process.

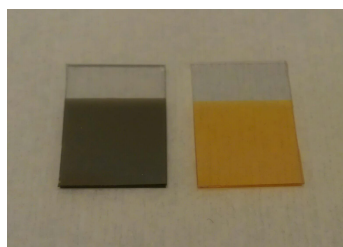


Figure 4.1: The sample to the left is coated with a thin 10 nm layer of Fe. The sample to the right is an Fe coated sample after annealing, where the red-orange Fe_2O_3 is obtained.

4.2 Deposition of overlayers

The three different overlayers FeOOH , NiOOH , and NiFeO_x were obtained by immersing the Fe_2O_3 samples in hot aqueous solutions that contained different chemicals for the different overlayers. The aqueous solutions were based on ultrapure Milli-Q water, and to deposit FeOOH overlayers, the solution contained 1 M NaNO_3 and 0.15 M $\text{FeCl}_3 \cdot 6\text{H}_2\text{O}$. For the NiOOH overlayers, the solution contained 1 M NaNO_3 and 0.15 M $\text{N}_2\text{NiO}_6 \cdot 6\text{H}_2\text{O}$, and for the NiFeO_x overlayer the solution contained 1 M NaNO_3 , 0.15 M $\text{FeCl}_3 \cdot 6\text{H}_2\text{O}$, and 0.15 M $\text{N}_2\text{NiO}_6 \cdot 6\text{H}_2\text{O}$.

The Fe_2O_3 films were immersed at different temperatures of the hot solution and for different durations in order to optimise the overlayer deposition. Different temperatures are expected to result in different structures of the overlayers, because the chemical composition of the hot solution changes as well as the deposition rate. Different durations are expected to result in different thicknesses of the overlayers, where a longer immersion time is expected to result in a thicker overlayer. After the deposition, the glass side of the samples were cleaned with isopropanol and the Fe_2O_3 /overlayer films were washed with excess of Milli-Q water and dried at room temperature for at least 12 hours. A schematic view of the Fe_2O_3 film with an overlayer is shown in figure 4.2.

To optimise the temperature, each overlayer were deposited in 60°C, 70°C, 80°C, 90°C, and 100°C for 5 minutes. Then, the optimised temperatures for each solution were used to optimise the time duration. The different deposition times were 1, 3, 5, 8, and 15 minutes.

4.3 Fabrication of electrodes

When designing an electrode, it is important to understand that only the Fe_2O_3 , or overlayer if there is one, should be in contact with the electrolyte. It will affect the charge transport in the PEC cell, and hence its performance, if the ITO or any other conducting component is in contact with the electrolyte.

A copper wire was used to get electrical contact between the ITO and the external circuit. The wire was first looped to increase the area in contact with the ITO. Then,

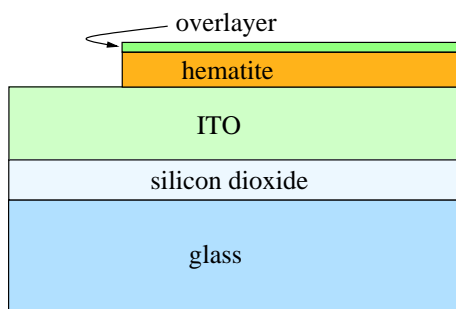


Figure 4.2: A schematic side view of the fabricated photo-anode samples. The thermal deposited overlayer is either FeOOH , NiOOH , or NiFeO_x . Note: not drawn to scale.

the loop was dipped in conducting silver paint and gently pressed against the ITO layer for a few seconds. The silver paint was then dried in room temperature for one hour.

To avoid contact between the copper wire and the electrolyte, the wire, except for its two ends, was placed in a glass tube. The loop, ITO, and parts of the Fe_2O_3 /overlayer film were sealed with glue from a glue gun to complete the electrode fabrication. Note that both glass and the glue are non-reactive and can be in contact with the electrolyte without affecting the performance of the PEC cell.

4.3.1 Active surface area

The part of the Fe_2O_3 /overlayer film that was not sealed with glue is called the active surface area, since this part was in contact with the electrolyte and therefore was used for water splitting. Two different methods of designing the active surface area were evaluated in this project.

The first method was the freehand design. The glue was applied without any forming tool, resulting in surface areas with irregular shapes and different areas for each electrode. The image processing software ImageJ was used to measure the active surface areas. To do this, a photo was taken with an electrode together with a ruler for scale. The active surface area was highlighted and measured using several threshold techniques in the software.

The second method was to have the same active surface area for each electrode. A cylindrical Teflon block was gently pressed against the Fe_2O_3 /overlayer film, and glue was applied around this block. The Teflon block was then removed when the glue had hardened, resulting in a circular active surface area with a known size.

Two electrodes, one for each method, are shown in figure 4.3. The two designs have both advantages and disadvantages. The freehand design is easier to fabricate, but the active surface areas differ from electrode to electrode, which requires the



Figure 4.3: The electrode to the left is designed with the freehand method, and the electrode to the right is designed with a circular Teflon block to obtain a circular active surface area.

image processing software. The only advantage with the Teflon block design is that the active surface areas are the same for all electrodes, which enables faster and easier comparisons between electrodes during measurements. However, several disadvantages have been noticed. First, the gluing process is complicated and there is a risk of not sealing the Fe_2O_3 /overlayer film properly, and instead creating cave-like structures underneath the glue. The electrolyte will enter these areas, and since the glue is partially transparent, some photons will reach the Fe_2O_3 /overlayer film where the unwanted electrolyte is, and water splitting will occur. Also, this design creates sharp edges between the Fe_2O_3 /overlayer film, glue, and electrolyte. These sharp edges make it more difficult for generated oxygen gas bubbles to leave the active surface area. The active surface area is decreased if small bubbles are stuck at the Fe_2O_3 /overlayer/electrolyte interface, resulting in a decreased performance of the PEC cell.

Overall, the freehand design was considered the best one. The image processing in ImageJ was not time consuming, and the current density (A/cm^2) in the PEC cell will not depend on the active surface area. After the design evaluation, all electrodes were fabricated with the freehand design.

5

Experimental Methods

The laboratory experiments in this project are divided into three parts: measurements in the PEC cell, Raman spectroscopy, and absorption spectroscopy. The main part is measurements in the PEC cell, including measurements of the generated photocurrent, electrochemical impedance spectroscopy, Mott-Schottky, and calculations of the surface charge separation efficiency.

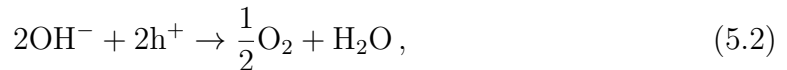
5.1 Measurements in the PEC cell

The PEC cell used in this project was a cell with three electrodes: a hematite working electrode, a platinum mesh counter electrode, and an Ag/AgCl in saturated KCl reference electrode. The three compartments in the cell, one for each electrode, were connected to each other via salt bridges. The compartment for the photoanode contained a quartz window to enable the UV radiation to reach the photoanode, since a PEC glass cell generally absorbs wavelengths below about 360 nm [28]. The reference electrode potential can be converted to the potential of a reversible hydrogen electrode, RHE, according to the Nernst equation:

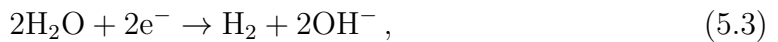
$$E_{\text{RHE}} = E_{\text{Ag/AgCl}} + E_{\text{Ag/AgCl}}^0 + 0.059 \cdot \text{pH}, \quad (5.1)$$

where $E_{\text{Ag/AgCl}}$ is the potential with respect to the Ag/AgCl electrode, $E_{\text{Ag/AgCl}}^0 = 0.197 \text{ V}$ in saturated KCl at 25°C , and the pH is of the electrolyte in the PEC cell [29]. The electrolyte used was 0.1 M NaOH , which is a strong base with a theoretical pH value of 13. So, for this particular electrolyte, the potential of the Ag/AgCl reference electrode is related to RHE according to $E_{\text{RHE}} = E_{\text{Ag/AgCl}} + 0.965$.

The water splitting reactions depend on the pH, and under alkaline conditions they are different from the ones presented in section 2.3 [30]. Here, the hydroxide groups in the electrolyte are involved in the water splitting reactions. The oxidation at the photo-anode generates oxygen gas according to



with the oxidation potential $-1.23 \text{ V}_{\text{RHE}}$ [28]. The reduction takes place at the cathode according to



and the reduction potential is 0 V_{RHE} [28]. Note that the net reaction is the same as before, in total one water molecule is split into oxygen gas and hydrogen gas.

5. Experimental Methods

As previously mentioned, an external bias potential is required to achieve water splitting. The applied potential is controlled by a Gamry Reference 600 potentiostat, which is connected to the electrodes in the PEC cell and to a computer. The potentiostat is an important instrument in this project since it is used for all the measurements performed in the PEC cell. The potentiostat is shown, together with the PEC cell, in figure 5.1.

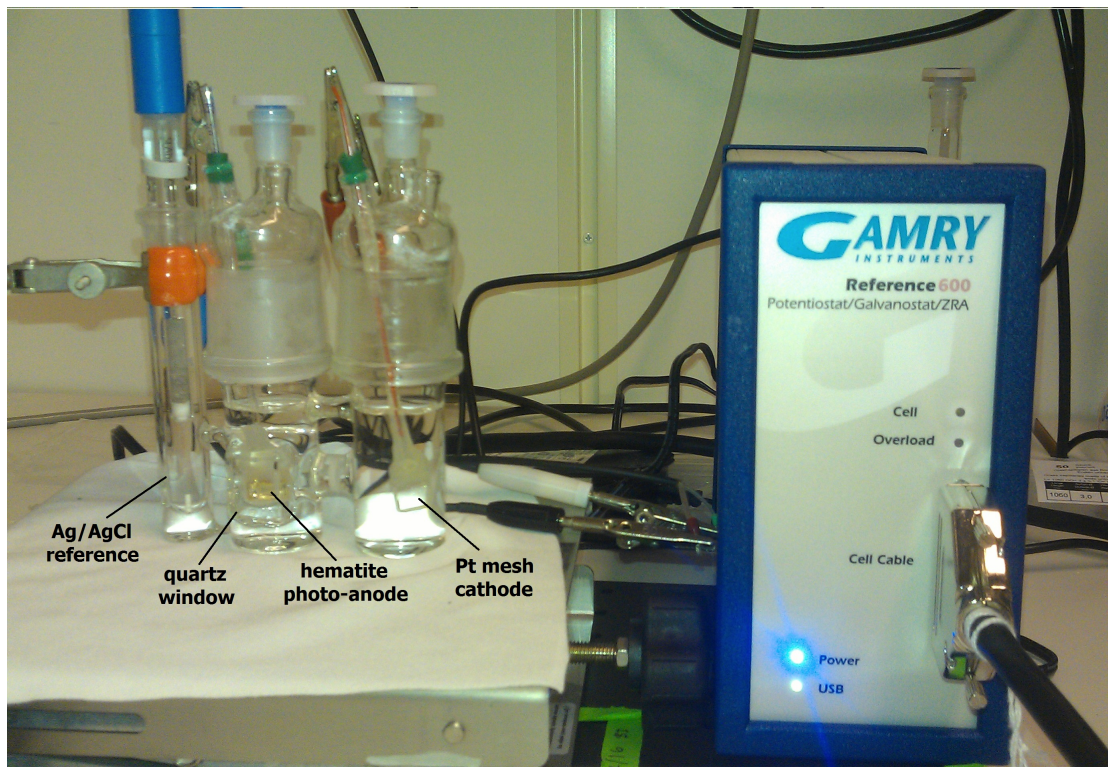


Figure 5.1: The PEC cell is shown to the left where each electrode is labelled. Note the quartz window that is required in order for the UV radiation to reach the photo-anode. The potentiostat, shown to the right, was used to control the applied bias voltage to the PEC cell during the measurements.

A solar simulator (SS150, Sciencetech Inc) was used to illuminate the photo-anodes. Since the real solar irradiation that reaches Earth's surface varies with for example the weather and angle of incidence, a standard spectrum has been developed. This standard spectrum is called air mass (AM) 1.5 G and corresponds to an intensity of $1\,000\text{ W/m}^2$. The air mass value denotes the amount of atmosphere through which the light has travelled, and the letter G stands for global and means that not only direct irradiation but also diffuse and reflected light is included in the spectrum [31]. A sun calibrated reference detector (Sciencetech Inc) was used to calibrate the distance between the solar simulator and the PEC cell.

5.1.1 Voltammetry

In voltammetry, the current is measured as the applied external bias potential is varied. The current is an indirect measure of the amount of oxygen and hydrogen

gas that is generated in the PEC cell. The Faraday efficiency is the efficiency with which the electrons take part in an electrochemical reaction, and it has been shown that the Faraday efficiency of the oxygen gas evolution in a PEC cell using an ultrathin Fe_2O_3 photo-anode is 100% [32]. An 100% Faraday efficiency in a PEC cell corresponds to that all electrons measured in the external circuit are used to generate hydrogen gas at the cathode, hence the current is a good measure of the performance of the PEC cell.

Especially two properties are of interest in voltammetry: the onset potential and the amount of photocurrent. The onset potential, E_{ons} , is the applied bias voltage at which the photocurrent starts. Since the need to apply a bias voltage to the PEC cell is unwanted, it is desired to have as low onset potential as possible. The amount of photocurrent does, as already mentioned, correspond to the amount of generated hydrogen gas. It is therefore desired to have a high photocurrent for as low applied bias voltages as possible. To compare the performance of electrodes, the measured current is divided by the active surface area to obtain a current density, denoted j . A combination of the onset potential and current density has been used to evaluate the performance of the different electrodes fabricated in this project.

Cyclic voltammetry was the method utilised to optimise the deposition of the overlayers. All fabricated electrodes were measured during 8 cycles, ranging between $-0.5 \text{ V}_{\text{Ag}/\text{AgCl}}$ and $+1 \text{ V}_{\text{Ag}/\text{AgCl}}$. The scan rate was 20 mV/s with 10 mV steps. The first 3 cycles were performed in dark, that is without any simulated sunlight, and the following 5 cycles were performed under AM 1.5 G simulated sunlight. Two half cycles where the applied bias voltage is increasing, one for dark mode and one for light mode, was then selected as a result for each electrode. The selected half cycles are from the latter part of each measurement, typically cycle 3 in dark mode and cycle 4 or 5 in light mode.

5.1.2 Electrochemical Impedance Spectroscopy

Electrochemical Impedance Spectroscopy (EIS) is a method to obtain information about the PEC cell by modelling the electrochemical process and measure the impedance. Impedance is a complex quantity that measures the ability to resist electrical current flow, and it can be written as

$$Z = Z_0 e^{j\theta}, \quad (5.4)$$

where $Z_0 = |Z|$ and θ is the phase shift between the voltage and the current. Note that the impedance of a resistor and of a capacitor are

$$Z_R = R, \quad \text{and} \quad Z_C = \frac{1}{j\omega C}. \quad (5.5)$$

Two different circuit models of the systems are commonly used, Hamann's circuit and Randle's simplified circuit [32], which are shown in figure 5.2. The two circuits have some common components: a series resistance R_s between the ITO layer and Fe_2O_3 , a bulk resistance R_{bulk} in Fe_2O_3 that is modelled in parallel with a bulk capacitance C_{bulk} . The bulk resistance is due to charge recombination of electrons and holes, and the bulk capacitance comes from the space charge region, explained in section 2.3.2.

Hamann's circuit also contains a surface-state capacitance C_{ss} and a surface-state resistance R_{ss} . C_{ss} is the capacitance of charges that are localised at surface states while R_{ss} corresponds to the charge transfer resistance between the Fe_2O_3 and the electrolyte [32]. If the oxidation at the Fe_2O_3 /overlayer/electrolyte interface occurs with holes that are directly transferred from the valence band, no charges are trapped at the Fe_2O_3 /overlayer/electrolyte interface, and Randle's simplified circuit should be more suitable than Hamann's circuit. However, there is still a surface-state resistance, but this has been included in the bulk resistance in Randle's simplified circuit.

To perform an EIS measurement in the PEC cell, an external bias voltage is applied together with a low AC voltage, whose frequency is varied. The result can be plotted in a Nyquist diagram, where the real part of the impedance is plotted on the x-axis and the imaginary part on the y-axis. To calculate the components of the circuit models, the spectrum plot must be curve fitted. In this project, EIS was measured under illumination for all electrodes. The applied bias voltage was 0.23 $V_{\text{Ag}/\text{AgCl}}$ and the amplitude of the AC voltage was 50 mV. The frequency range was between 100 kHz and 0.1 Hz and the spectra were curve fitted in the potentiostat software.

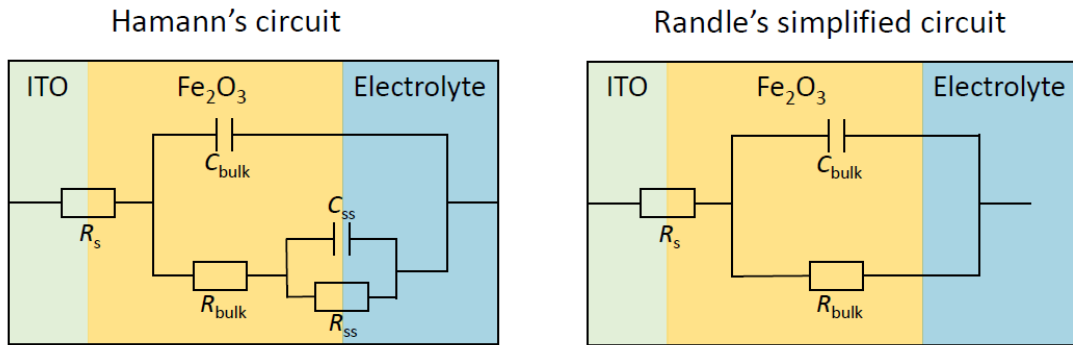


Figure 5.2: Two circuit models for the PEC cell: Hamann's circuit and Randle's simplified circuit. The two models have the same Fe_2O_3 bulk components and the same ITO/ Fe_2O_3 series resistance, but differ in that way that Hamann's circuit includes a surface-state capacitance in parallel with a surface-state resistance.

5.1.3 Mott-Schottky analysis

Mott-Schottky (MS) analysis is a method to calculate C_{bulk} in the circuit models presented above. The MS equation is

$$\left(\frac{A}{C_{\text{bulk}}}\right)^2 = \frac{2}{\epsilon_r \epsilon_0 e N_D} \left(E - E_{\text{fb}} - \frac{k_B T}{e}\right), \quad (5.6)$$

where C_{bulk} is the capacitance of the space charge region, A is the active surface area, ϵ_r is the dielectric constant, ϵ_0 is the permittivity of vacuum, e is the elementary charge, N_D is the charge carrier concentration, E is the applied voltage, E_{fb} is the flat-band potential, k_B is the Boltzmann constant, and T is the absolute temperature [28]. The validity of the MS equation depends on three assumptions.

Firstly, there are two capacitances to consider, the space charge region in the Fe_2O_3 and a Helmholtz double layer in the electrolyte. These are in series, and in order for the contribution of the Helmholtz double layer to be negligible, its capacitance must be much larger than C_{bulk} . Secondly, the charge carriers must be evenly distributed in space and be all ionised. At last, the width of the space charge region must be much smaller than the width of the semiconductor [33].

In a Mott-Schottky plot, $(A/C_{\text{bulk}})^2$ is plotted as a function of the applied potential. If the three assumptions mentioned above are fulfilled, the MS plot will be linear and the charge carrier concentration can be calculated from

$$N_{\text{D}} = \frac{2}{\varepsilon_{\text{r}}\varepsilon_0 e S}, \quad (5.7)$$

where S is the slope of the MS plot [33]. Besides that, the flat-band potential can be calculated by extrapolation of the MS plot to the intersection with the x-axis. At the intersection, the relationship

$$E_{\text{fb}} = E - \frac{k_{\text{B}}T}{e} \quad (5.8)$$

is used to obtain the flat-band potential.

All MS measurements were performed in dark, and the applied bias voltage was increased from $-0.8 \text{ V}_{\text{Ag}/\text{AgCl}}$ to $+0.5 \text{ V}_{\text{Ag}/\text{AgCl}}$ using a step size of 10 mV. The AC voltage amplitude and frequency were 50 mV and 1 kHz, respectively.

5.1.4 Surface charge separation efficiency

In this section, a technique for calculation of the surface charge separation efficiency is presented. The photocurrent density in an aqueous electrolyte can be written

$$j_{\text{H}_2\text{O}} = j_{\text{max}}\eta_{\text{abs}}\eta_{\text{sep}}\eta_{\text{surf}}, \quad (5.9)$$

where $j_{\text{H}_2\text{O}}$ is the measured photocurrent, j_{max} is the maximum photocurrent, η_{abs} is the light absorption efficiency, η_{sep} is the charge separation efficiency, and η_{surf} is the surface charge separation efficiency [11]. If hydrogen peroxide, H_2O_2 , is present in the electrolyte, the oxidation kinetics is high and $\eta_{\text{surf}} = 1$ is assumed. This gives the photocurrent in the modified electrolyte

$$j_{\text{H}_2\text{O}_2} = j_{\text{max}}\eta_{\text{abs}}\eta_{\text{sep}}, \quad (5.10)$$

and η_{surf} can be obtained from

$$\frac{j_{\text{H}_2\text{O}}}{j_{\text{H}_2\text{O}_2}} = \eta_{\text{surf}}. \quad (5.11)$$

In this project, $j_{\text{H}_2\text{O}_2}$ was measured for the optimised overlayers in an electrolyte containing 0.1 M NaOH and 0.3 M H_2O_2 . Otherwise the measurements were identical from the voltammetry presented in section 5.1.1.

5.2 Raman spectroscopy

Raman spectroscopy is a method to identify molecules by analysing inelastic scattering of photons. The method is based on the fact that molecules have quantized vibrational energy states, $v = 0, 1, 2, 3, \dots$, that are unique for each type of molecule. When a photon of visible light, that has a too low energy to excite an electron in the molecule, interacts with the molecule it can be scattered in three different ways: Rayleigh scattering, Stokes Raman scattering, and anti-Stokes Raman scattering, all shown in figure 6.10 [34]. The scattering process of a photon begins with absorption of the photon energy to a virtual energy level in the molecule. A photon is then re-emitted when the molecule is deexcited back to a real energy state. If the initial and final energy states are the same, that is the vibrational number v is unchanged, the scattering is elastic and the photon energy is conserved. This is called Rayleigh scattering, and it is the most common one of the three possible processes [34]. The second scattering process is if the final vibrational energy state is higher than the initial energy state, which is called Stokes Raman scattering. This means that the molecule has absorbed some of the photon energy, and the scattered process is inelastic. The third process is called anti-Stokes Raman scattering, and it occurs if the molecule initially is excited to a higher vibrational level, and the final energy state has a lower vibrational number, which means that the molecule has lost some of its energy to the photon.

The Raman shift due to Stokes and anti-Stokes Raman scattering is typically

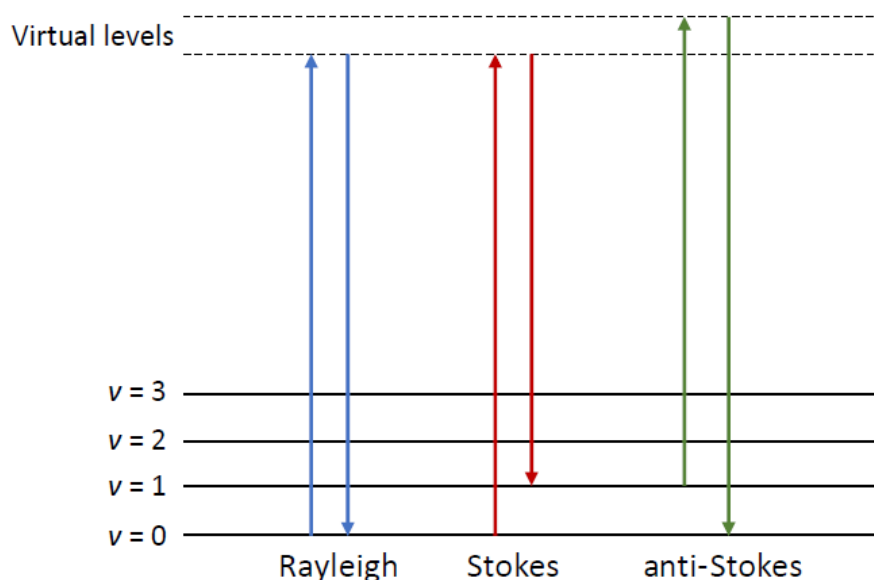


Figure 5.3: The energy levels and scattering processes that are included in Raman spectroscopy. Rayleigh scattering is an elastic process that is more common than the other two. However, Stokes and anti-Stokes inelastic scattering includes energy changes in the scattered photon, which in Raman spectroscopy are used to identify the molecules because each molecule has its unique energy states.

presented in wavenumbers $\tilde{\nu}$ in the unit cm^{-1} , which corresponds the number of wavelengths per cm. This value is related to the energy difference between the incident and the scattered photon, according to

$$\tilde{\nu} = \frac{1}{\lambda_{\text{in}}} - \frac{1}{\lambda_{\text{sc}}}, \quad (5.12)$$

where λ_{in} is the wavelength of the incident photon and λ_{sc} is the wavelength of the scattered photon. Note that the wavelengths must be in cm to obtain the wavenumber unit cm^{-1} .

Measurements were performed to identify the molecules in Fe_2O_3 and the overlayers. Samples with ITO/ Fe_2O_3 /overlayers were measured as well as samples directly from the aqueous solutions that were used for overlayer deposition. These samples were prepared by applying a few droplets of the aqueous solutions on a cleaned ITO sample and let the droplets dry at room temperature overnight. This was done for all three solutions at the temperatures 60°C , 70°C , 80°C , 90°C , and 100°C . The Raman microscope that was used was WITec alpha300 R with a 488 nm laser. A spectrum was obtained by accumulation of 50 spectra, each with an integration time of 1 s.

5.3 Light absorption spectroscopy

The band gap of the hematite was analysed by measuring the light transmission as a function of wavelength using a Cary 5000 UV-Vis-NIR spectrophotometer. The principle behind a light transmission measurement is to compare the intensity of two monochromatic light beams, one that passes through the sample of interest and one that is used as a reference intensity. An ITO sample was used as a baseline correction, and assuming no light scattering occurs at either the ITO/ Fe_2O_3 interface or at the Fe_2O_3 /overlayer interface, the adsorption A is given as

$$A = 1 - T, \quad (5.13)$$

where T is the measured transmission. Measurements were performed in the interval 300 – 800 nm with a scan rate of 600 nm/min and a step size of 1 nm. A pure Fe_2O_3 sample was measured as well as the three optimised overlayers.

6

Result and discussion

The result section is structured in the following way: first the deposition of the three overlayers FeOOH, NiOOH, and NiFeO_x is optimised both in deposition time and temperature of the aqueous solution. The optimised electrodes are then compared to each other by the methods described in chapter 5.

6.1 Optimisation of overlayer deposition

The optimisation is done for each of the three different overlayers: FeOOH, NiOOH, and NiFeO_x. Note that voltammetry was the only method used to optimise the overlayers.

6.1.1 FeOOH overlayer

First, the temperature of the aqueous solution was varied, and the result is shown in left panel of figure 6.1. The current density is increased for the temperatures 60 – 80°C, and it is clear that the two temperatures 70°C and 80°C give the highest photocurrent densities and the lowest onset potentials. However, 80°C is considered the optimised temperature of the aqueous solution due to the higher current density at applied bias voltages above 1.2 V_{RHE}.

The optimisation of deposition time is shown in the right panel of figure 6.1. All deposition times improve the performance of the photo-anode. The shorter deposition time, the better performance is observed. To conclude, the optimised deposition is 1 min in an 80°C solution. As mentioned previously, the onset potential is an important parameter for Fe₂O₃ photo-anodes. In this project, the onset potential is defined as the applied bias voltage where the photocurrent density exceeds 20 μA/cm². The onset potentials for all electrode used for FeOOH deposition are shown in table 6.1. For the optimised deposition, the onset potential is lowered by 220 mV, from 1150 mV_{RHE} for bare Fe₂O₃ to 930 mV_{RHE} for the FeOOH overlayer.

Note the difference between the two bare Fe₂O₃ electrodes in figure 6.1. Their onset potentials differ as well as their current densities. The two optimisation experiments were performed with samples from different Fe depositions in the Lesker evaporator. Since other elements are used in the evaporator, there is a risk that previously evaporated elements are deposited together with the Fe. This may cause doping of the Fe₂O₃ electrodes, which changes their performance. To compare different electrodes with each other, there is therefore of great importance that they are fabricated under the same conditions, which they are in this project.

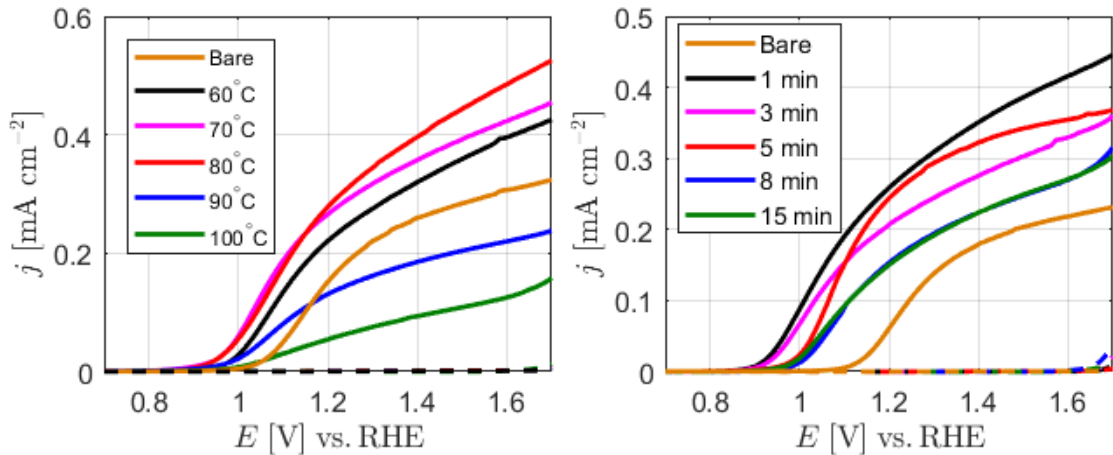


Figure 6.1: Optimisation of FeOOH overlayer deposition. **Left panel:** optimisation of deposition temperature. The deposition was 5 min for all samples, and 80°C is considered the optimised temperature. **Right panel:** optimisation of deposition time. All overlayers were deposited at 80°C, and the shortest deposition time of 1 min gives the highest current density and lowest onset potential. Dashed lines represent dark currents. Note that these two measurements were performed with electrodes from different Fe depositions in the Lesker evaporator, hence they differ from each other.

Table 6.1: The onset potentials E_{ons} for the electrodes used for optimisation of FeOOH overlayers. The onset potential is here defined as the applied bias voltage where the photocurrent density exceeds $20 \mu\text{A}/\text{cm}^2$.

Deposition temperature	Bare	60°C	70°C	80°C	90°C	100°C
E_{ons} [mV _{RHE}]	1060	980	950	950	990	1060
Deposition time	Bare	1 min	3 min	5 min	8 min	15 min
E_{ons} [mV _{RHE}]	1150	930	940	990	1020	1000

Overall, the FeOOH deposition is successful and improves the performance of the Fe₂O₃ photo-anode. It is clear that a longer deposition time gives a decreased photocurrent density, and a possible explanation for this is that the overlayers are too thick. The overlayer increases the diffusion path of the holes generated in the Fe₂O₃, and its advantage with the surface passivation must be weighted against the increased diffusion path, hence too thick films are inefficient. The same conclusion has also been drawn by Kim et al. [10], although they used a deposition temperature of 100°C and found an optimised deposition time of 5 min. A possible explanation for the differences seen in the optimisation of the temperature is the kinetics of the chemical reactions in the solution at different temperatures. It has been reported that several chemical reactions occur during thermal deposition of FeOOH in an aqueous solution, and their kinetics are temperature dependent [35]. During the thermal deposition, it was observed that the aqueous solution changed appearance at around 80°C, from a clear to a more cloudy solution. Anyhow, the whole deposition process is complicated and a detailed study of it is beyond the scope of this project.

6.1.2 NiOOH overlayer

The optimisation of the NiOOH overlayer took place in the same way as for the FeOOH overlayer. The result from the temperature optimisation is shown in the left panel of figure 6.2. The current densities are increased, and the onset potentials are decreased, for all electrodes compared to the bare Fe_2O_3 electrode. Since the temperature 60°C gives the lowest onset potential, it is considered the optimised temperature. No clear connection between the temperature and photocurrent density is found, but it is found that the onset potential is increased with increasing temperature, which appears more clearly in table 6.2 that shows the onset potentials.

The deposition time optimisation is shown in the right panel of figure 6.2. All deposition times give similar results, but 5 min is considered the optimised deposition time due to the lowered onset potential. All NiOOH overlayer electrodes show an improved performance as photo-anodes compared to the bare Fe_2O_3 electrode. For the optimised deposition, the onset potential is decreased by 90 mV, from 1150 mV_{RHE} for the bare Fe_2O_3 electrode to 1060 mV_{RHE}. However, no clear connection between deposition time and photocurrent is observed. A possible explanation is that the deposition rate decreases with increasing film thickness, so all deposited films have more or less the same thickness.

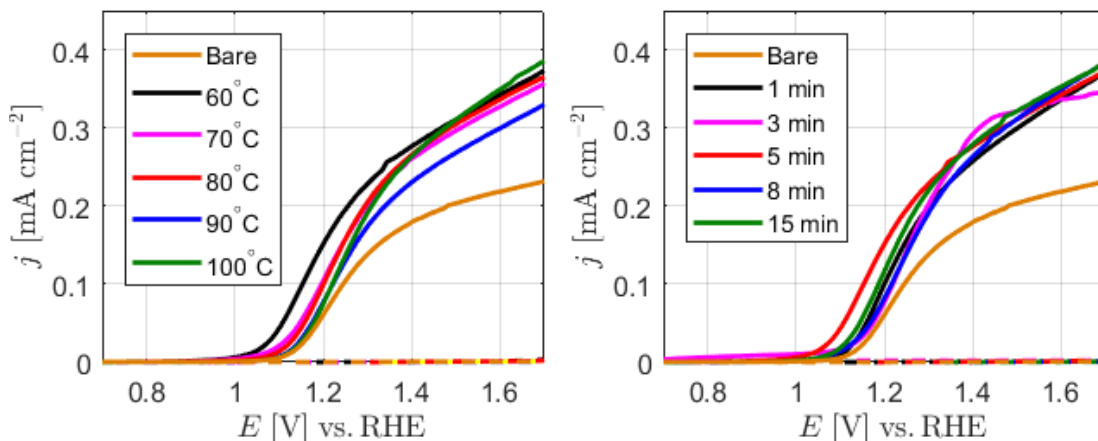


Figure 6.2: Optimisation of NiOOH overlayer deposition. **Left panel:** optimisation of deposition temperature. The deposition was 5 min for all samples, and 60°C is considered the optimised temperature, especially due to the lowered onset potential. **Right panel:** optimisation of deposition time. All overlayers were deposited at 60°C , and the deposition time of 5 min gives the lowest onset potential and highest photocurrent density at low applied voltages. Dashed lines represent dark currents.

6.1.3 NiFeO_x overlayer

The optimisation of the NiFeO_x overlayer took place in the same way as for FeOOH and NiOOH. The left panel of figure 6.3 shows the temperature optimisation, and table 6.3 shows the onset potentials. It is seen that the deposition temperatures 90°C

Table 6.2: The onset potentials E_{ons} for the electrodes used for optimisation of NiOOH overlayers. The onset potential is here defined as the applied bias voltage where the photocurrent density exceeds $20 \mu\text{A}/\text{cm}^2$.

Deposition temperature	Bare	60°C	70°C	80°C	90°C	100°C
E_{ons} [mV _{RHE}]	1150	1060	1100	1120	1140	1140
Deposition time	Bare	1 min	3 min	5 min	8 min	15 min
E_{ons} [mV _{RHE}]	1150	1120	1120	1060	1120	1100

and 100°C have the lowest onset potentials, and since the electrode from the 90°C deposition shows the highest photocurrent density, it is considered the optimised deposition temperature.

The optimisation of deposition time is shown in the right panel of figure 6.3. The same result as for the FeOOH overlayer is observed; longer deposition times give less improvements of the photo-anodes. However, all photo-anodes with a NiFeO_x overlayer are improved compared to the bare Fe₂O₃ electrode. The optimised deposition time is considered to be 1 min, which is because of its low onset potential. Note that both 3 min and 5 min show higher current densities at large applied potentials, but their onset potentials are significantly higher compared to the 1 min deposition. For the optimised deposition, the onset potential is decreased by 100 mV, from 1150 mV_{RHE} for the bare Fe₂O₃ electrode to 1050 mV_{RHE}.

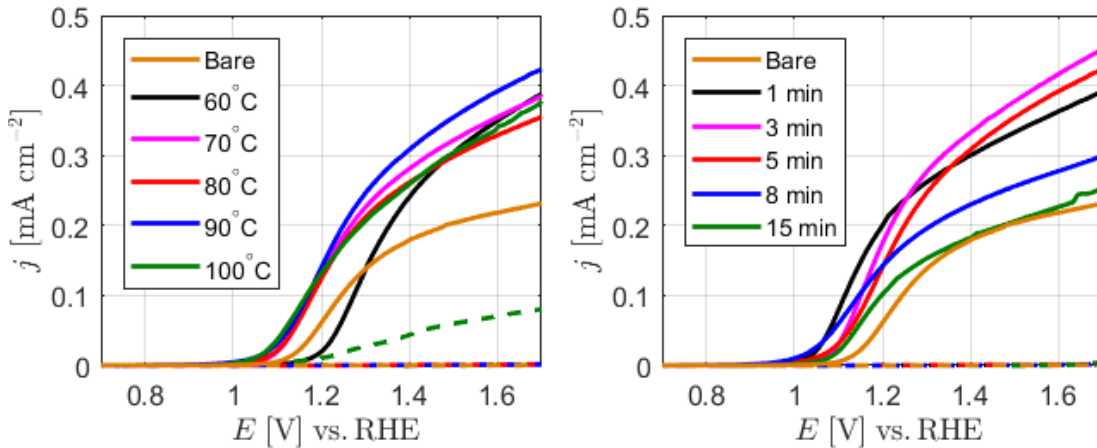


Figure 6.3: Optimisation of NiFeO_x overlayer deposition. **Left panel:** optimisation of deposition temperature. The deposition was 5 min for all samples, and 90°C is considered the optimised temperature. Note the surprisingly high dark current for the 100°C electrode, and the reason for this is unknown. **Right panel:** optimisation of deposition time. All overlayers were deposited at 90°C, and the shortest deposition time of 1 min shows the best combination of onset potential and current density at low applied bias voltages. Dashed lines represent dark currents.

Table 6.3: The onset potentials E_{ons} for the electrodes used for optimisation of NiFeO_x overlayers. The onset potential is here defined as the applied bias voltage where the photocurrent density exceeds $20 \mu\text{A}/\text{cm}^2$.

Deposition temperature	Bare	60°C	70°C	80°C	90°C	100°C
E_{ons} [mV _{RHE}]	1150	1200	1100	1100	1080	1080
Deposition time	Bare	1 min	3 min	5 min	8 min	15 min
E_{ons} [mV _{RHE}]	1150	1050	1090	1080	1040	1100

6.2 Comparison between FeOOH, NiOOH, and NiFeO_x overlayers

In this section, the optimised overlayers are compared to each other regarding current densities, EIS, MS, surface charge separation, and light absorption. The optimised deposition parameters for each overlayer are shown in table 6.4.

Table 6.4: The optimised thermal deposition parameters from section 6.1.

Overlayer	Temperature	Time
FeOOH	80°C	1 min
NiOOH	60°C	5 min
NiFeO_x	90°C	1 min

6.2.1 Voltammetry

Figure 6.4 shows a current density comparison between the three optimised overlayers. The photocurrent densities and the onset potentials are improved significantly compared to a bare Fe_2O_3 photo-anode. The FeOOH overlayer gives the best result, the onset potential is lowest and the photo-anode shows the highest current density for all applied voltages. The shift in onset potential of 220 mV is more than twice as much as the shift for the NiOOH and NiFeO_x overlayers. The overlayers NiOOH and NiFeO_x show similar performances. Their onset potentials are more or less the same, but the NiFeO_x overlayer shows a slightly higher photocurrent density. At the applied bias voltage $1.23 V_{\text{RHE}}$, the photocurrent density of the Fe_2O_3 -FeOOH photo-anode is increased by 211% compared to the Fe_2O_3 photo-anode. The corresponding improvements for the other photo-anodes are 102% for Fe_2O_3 -NiOOH and 155% for Fe_2O_3 - NiFeO_x .

6.2.2 Electrochemical Impedance Spectroscopy

The EIS measurements are shown as Nyquist diagrams in figure 6.5. All four curves are curve fitted to Hamann's circuit. A capacitor has the shape of a semicircle in a Nyquist diagram, so Hamann's circuit should be used when two semicircles are observed and Randle's simplified circuit should be used when one semicircle is observed. The two semicircles are easily seen for the bare Fe_2O_3 photo-anode, while

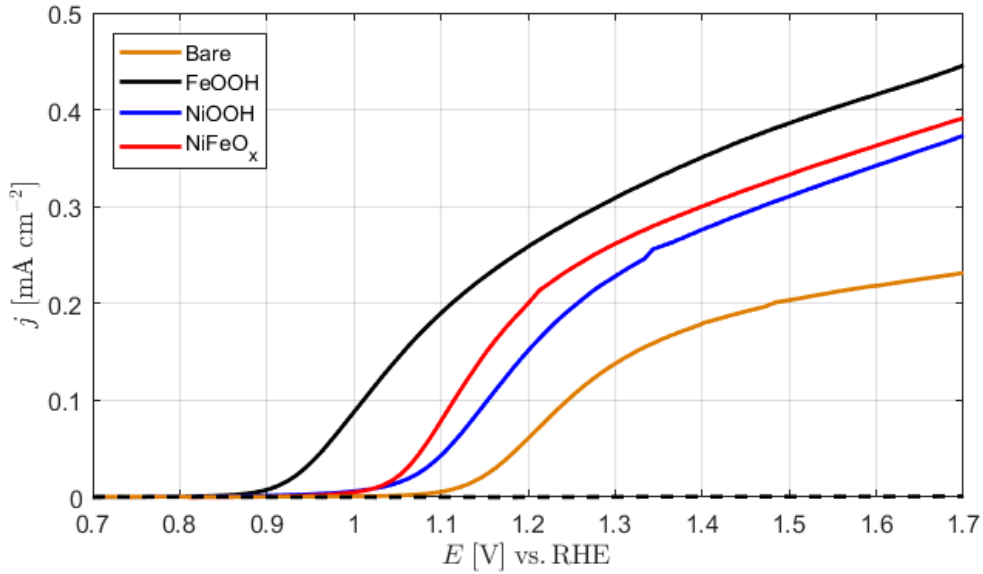


Figure 6.4: The photocurrent densities for Fe_2O_3 photo-anodes with the three different overlayers FeOOH, NiOOH, and NiFeO_x under 1 sun irradiation. The dashed lines are currents in dark.

the second semicircle is more difficult to see for the other photo-anodes, especially for Fe_2O_3 -FeOOH. However, since the shape of the Fe_2O_3 -FeOOH is different from only one semicircle, and the use of Hamann’s circuit at the applied bias voltage 1.23 V_{RHE} for Fe_2O_3 photo-anodes has been reported before [29], Hamann’s circuit was selected for all four photo-anodes. The curve fitting gives the fitted values for the resistances and capacitances in Hamann’s circuit, and these are shown in table 6.5. In general, the curve fitting resulted in relative large errors, hence there is a large margin of errors for these values.

The resistance R_s is similar for the four photo-anodes, which is expected since the resistance at the ITO/ Fe_2O_3 interface should not be affected by an overlayer located at the Fe_2O_3 /electrolyte interface. The bulk resistance, R_{bulk} , is increased for all overlayers compared to bare the Fe_2O_3 photo-anode. This would indicate an increased electron-hole recombination rate in the bulk, which could be due to the higher photocurrent density observed for the overlayer photo-anodes at 1.23 V_{RHE} . The values of R_{bulk} are changed in the same way as the photocurrent densities, highest for Fe_2O_3 -FeOOH and lowest for bare Fe_2O_3 . The third resistance parameter, R_{ss} , corresponds to the recombination rate at the Fe_2O_3 /overlayer/electrolyte interface. R_{ss} are lower for all overlayer photo-anodes, indicating the surface passivation and co-catalyst role of the overlayers.

The capacitance C_{bulk} is increased for the overlayer photo-anodes, which would indicate an increased charge separation in the space charge region, which in turn could be a result of a shifted flat-band potential. A decreased flat-band potential for the overlayer photo-anodes means that the applied bias voltage is further away from the flat-band potential, hence the band bending is increased. The second capacitance C_{ss} is increased for the NiOOH and NiFeO_x overlayers, while it is almost the same

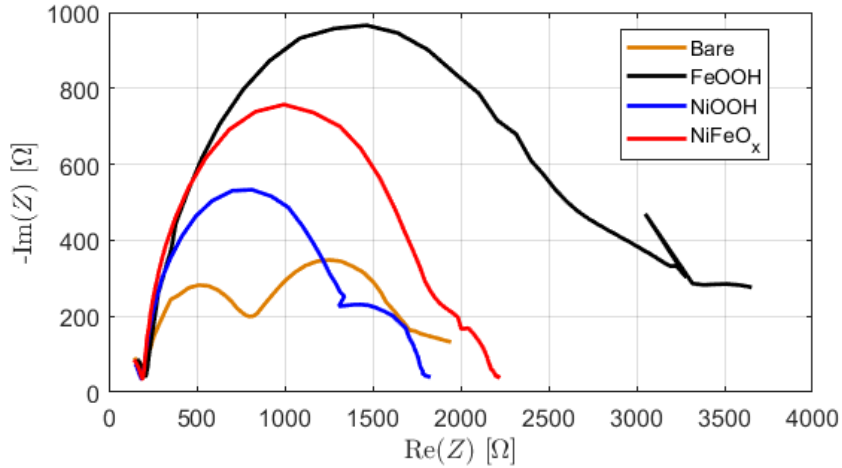


Figure 6.5: Nyquist diagrams for EIS measurements under 1 sun irradiation on four different photo-anodes: bare Fe_2O_3 , $\text{Fe}_2\text{O}_3\text{-FeOOH}$, $\text{Fe}_2\text{O}_3\text{-NiOOH}$, and $\text{Fe}_2\text{O}_3\text{-NiFeO}_x$. The applied bias voltage is $0.23 V_{\text{Ag}/\text{AgCl}} \approx 1.23 V_{\text{RHE}}$, and the frequency range is 0.1 Hz – 100 kHz.

Table 6.5: Values of resistances and capacitances in Hamann’s circuit obtained by curve fitting of the Nyquist diagrams in figure 6.5.

Overlayer	Bare	FeOOH	NiOOH	NiFeO _x
R_s [Ω]	190	210	190	190
R_{bulk} [$\Omega \text{ cm}^2$]	480	960	600	820
R_{ss} [$\Omega \text{ cm}^2$]	670	529	260	210
C_{bulk} [$\mu\text{F cm}^{-2}$]	0.90	1.20	1.30	1.40
C_{ss} [$\mu\text{F cm}^{-2}$]	50	40	110	130

for $\text{Fe}_2\text{O}_3\text{-FeOOH}$ and Fe_2O_3 . A higher C_{ss} could be a result of more holes at surface states, which is the result from a higher photocurrent. However, a low C_{ss} could either result from a low photocurrent or that a higher proportion of the holes that take part in the oxidation reaction comes directly from the valence band. As discussed above, the shape of the $\text{Fe}_2\text{O}_3\text{-FeOOH}$ Nyquist curve is unclear and more measurements are needed for further discussion.

6.2.3 Mott-Schottky

The result from the MS measurement is shown in figure 6.6, where the MS equation (5.6) is plotted as a function of the applied bias voltage. The MS plots are not linear, which means that the three assumptions mentioned in section 5.1.3 are not fulfilled. However, the graphs appear to be linear in the interval $1.0 - 1.2 V_{\text{RHE}}$, and the data in this interval is fitted to a linear plot in order to estimate the flat-band potentials of the photo-anodes. The flat-band potentials are estimated according to the relationship mentioned in section 5.1.3 and the result is shown in table 6.6. The flat-band potentials are lowered by 160 – 180 mV for the overlayers compared to the bare Fe_2O_3 photo-anode, which is consistent with the increased values of C_{bulk}

obtained under illumination in the EIS measurements, see table 6.5.

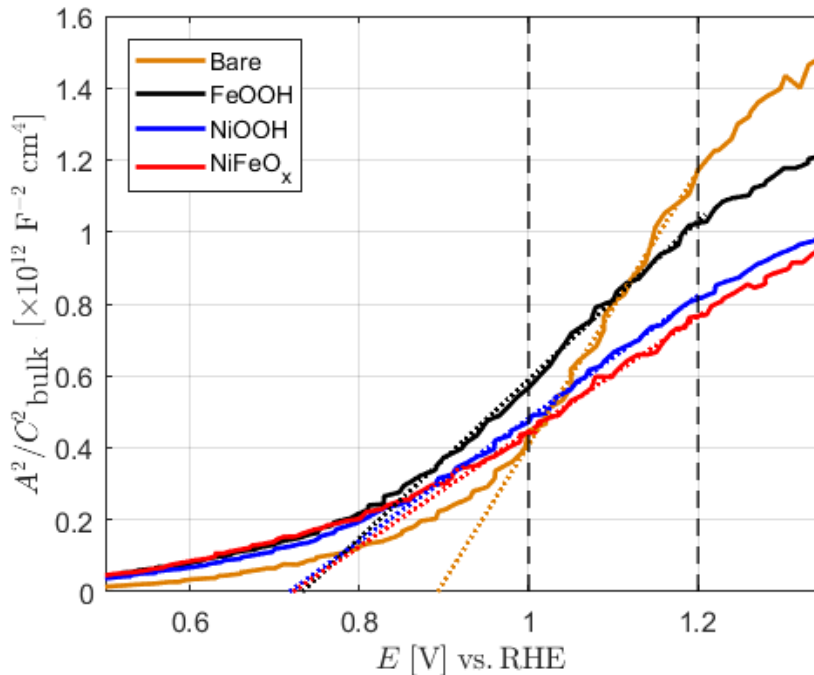


Figure 6.6: Mott-Schottky measurements in dark for the different photo-anodes bare Fe_2O_3 , $\text{Fe}_2\text{O}_3\text{-FeOOH}$, $\text{Fe}_2\text{O}_3\text{-NiOOH}$, and $\text{Fe}_2\text{O}_3\text{-NiFeO}_x$ obtained at 1 kHz. Linear plots are extrapolated from the interval 1.0 – 1.2 V_{RHE} and plotted as dotted lines to estimate the flat-band potentials of the different photo-anodes.

Table 6.6: The estimated flat-band potentials from the Mott-Schottky measurement.

Overlayer	Bare	FeOOH	NiOOH	NiFeO _x
E_{fb} [mV _{RHE}]	870	710	690	700

6.2.4 Surface charge separation

Figure 6.7 shows the comparison between the current densities obtained in the ordinary 0.1 M NaOH electrolyte and in an electrolyte that contained an addition of 0.3 M H_2O_2 . Overall, the onset potential is lowered significantly and the photocurrent densities are increased with the addition of H_2O_2 . From these curves, the charge separation efficiency for each photo-anode are calculated according to $\eta_{\text{surf}} = j_{\text{H}_2\text{O}}/j_{\text{H}_2\text{O}_2}$, and the result is shown in figure 6.8. The surface charge separation efficiency is highest for the $\text{Fe}_2\text{O}_3\text{-FeOOH}$ and $\text{Fe}_2\text{O}_3\text{-NiFeO}_x$ photo-anodes, while the NiOOH overlayer does not improve the charge separation efficiency noticeably compared to the bare Fe_2O_3 photo-anode.

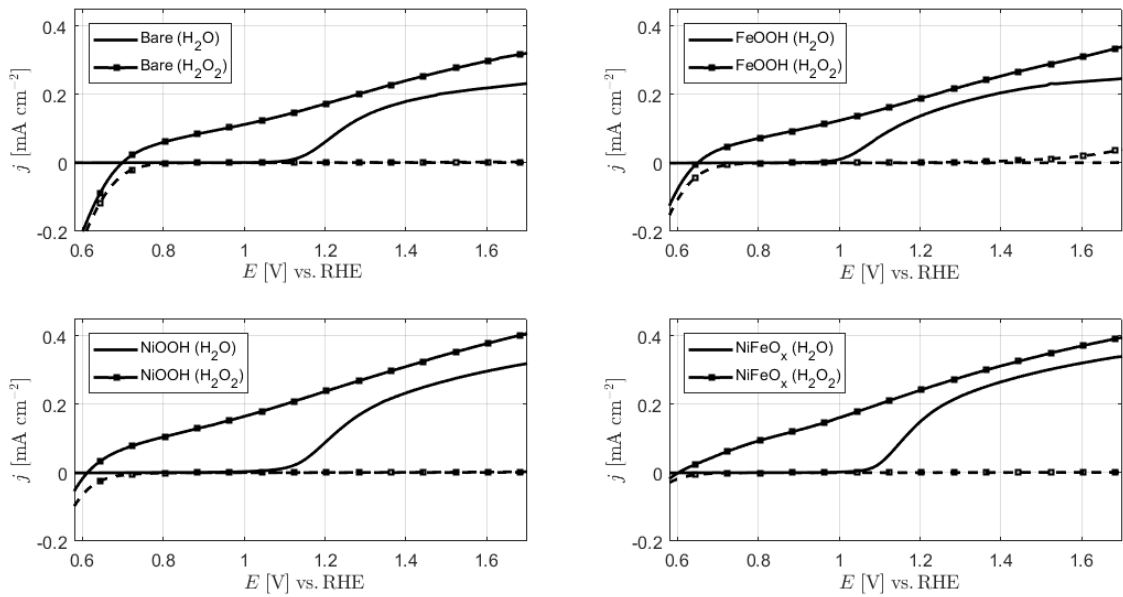


Figure 6.7: Comparison between the current densities obtained in 0.1 M NaOH and 0.1 M NaOH + 0.3 M H₂O₂ electrolyte. **Upper left panel:** comparison for bare Fe₂O₃ photo-anode. **Upper right panel:** comparison for Fe₂O₃-FeOOH photo-anode. **Lower left panel:** comparison for Fe₂O₃-NiOOH photo-anode. **Lower right panel:** comparison for Fe₂O₃-NiFeO_x photo-anode. Note that the photocurrents obtained in the 0.1 M NaOH electrolyte differ from the ones presented in figure 6.4, which is due to instability issues with the photo-anodes. Dashed lines represent dark currents.

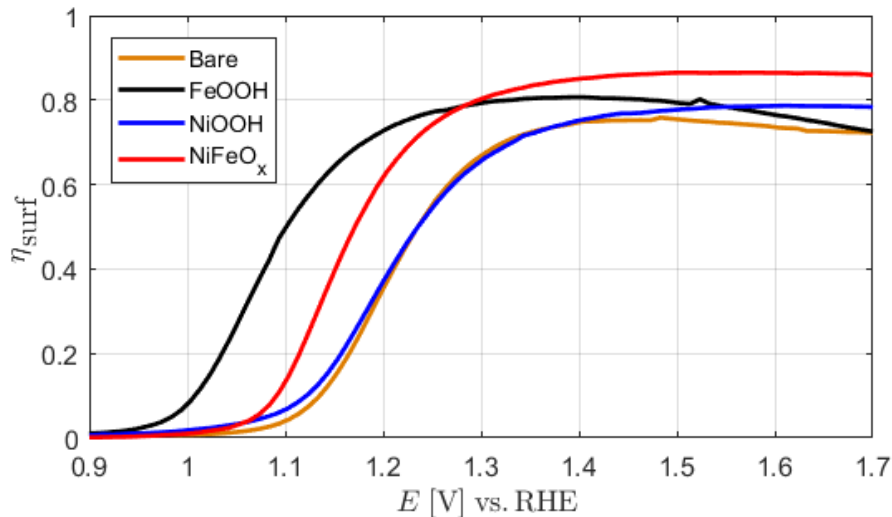


Figure 6.8: Surface charge transfer efficiency η_{surf} as a function of the applied bias voltage. The surface charge separation efficiency is, especially at low applied bias voltages, increased for the FeOOH and NiFeO_x overlayers. Note that the NiOOH overlayer, unlike to the other two overlayers, does not increase the surface charge separation efficiency significantly.

6.2.5 Light absorption

The light adsorption spectra for the photo-anodes are shown in figure 6.9. There are no significant differences between bare Fe_2O_3 photo-anode and the photo-anodes with deposited overlayers, which most likely is because the deposited overlayers are ultrathin. A FeOOH overlayer deposited during 5 min with a similar deposition method has been reported to have a thickness of 2 nm [10]. This shows that the increased performance of the overlayer photo-anodes is not a result of increased light absorption.

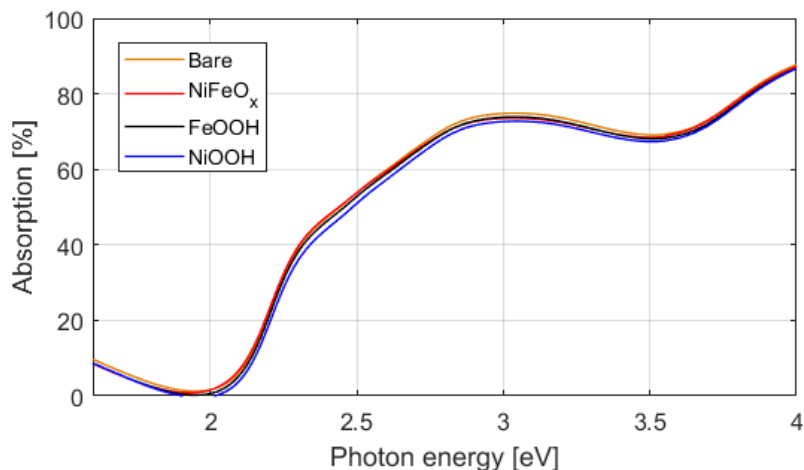


Figure 6.9: Absorption spectra as a function of photon energy for the three optimised overlayer photo-anodes and a bare Fe_2O_3 photo-anode. Note the bandgap of Fe_2O_3 that is located around 2 eV.

6.3 Raman spectroscopy

The Raman measurements did not show any differences between photo-anodes with different overlayers. This is probably because the overlayers are ultrathin, so any signal from the overlayers would be too low to notice. The samples directly from the aqueous solutions did not show any clear differences between each other, and Raman peaks reported for FeOOH [36] and NiOOH [37] are not present in the spectra. However, peaks in a bare Fe_2O_3 sample were observed, see figure 6.10, and they agree well with the peaks reported for Fe_2O_3 [36].

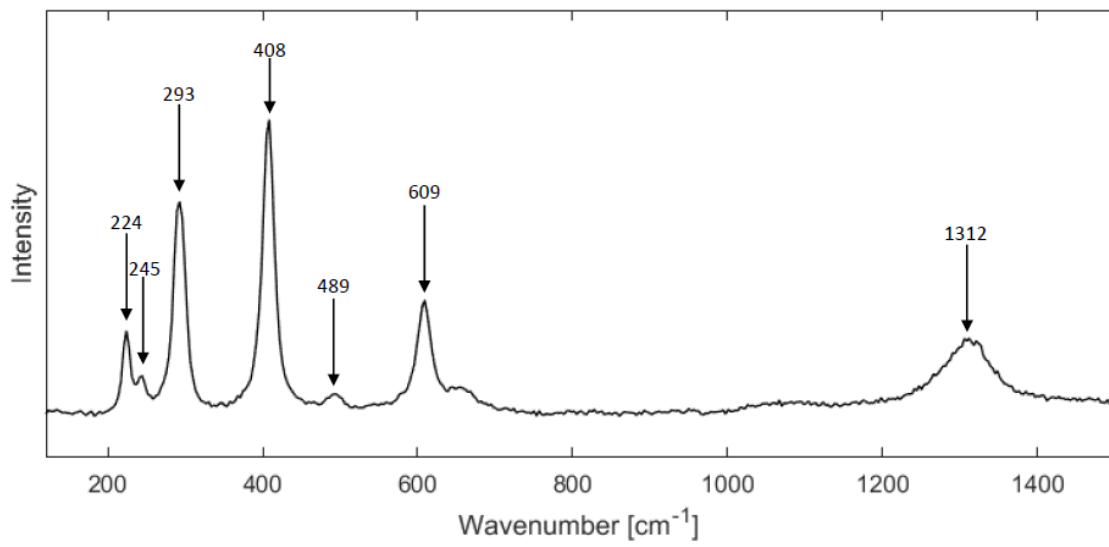


Figure 6.10: Raman shifts for a bare Fe_2O_3 photo-anode. Several peaks are observed and they are consistent with reported peaks for Fe_2O_3 .

7

Conclusion

This Master's thesis has analysed the ability to improve the photoelectrochemical hydrogen generation from water splitting using ultrathin overlayers on Fe_2O_3 photo-anodes. Three different overlayers were deposited on Fe_2O_3 samples; FeOOH , NiOOH , and NiFeO_x . The Fe_2O_3 samples were immersed in a hot, aqueous solution containing different chemicals in order to deposit an ultrathin overlayer. All three overlayers were deposited successfully, and the two deposition parameters temperature of the aqueous solution and deposition time were optimised for each overlayer. All three overlayers showed an increased photocurrent density as well as a decrease in the onset potential compared to the bare Fe_2O_3 photo-anode. Improvements of these two, very important parameters in a PEC cell, shows the potential for ultrathin overlayers to be further investigated in the future.

The three different overlayers were also compared to each other in a series of measurements. The Fe_2O_3 - FeOOH photo-anode gave the highest measured photocurrent density and the lowest onset potential. Overall, the three overlayers showed similar differences to the bare Fe_2O_3 photo-anode, for examples the lowering of the flat-band potential, onset potential, surface state resistance, and increasing of photocurrent density, surface charge separation efficiency, bulk resistance, etcetera.

An issue that has been dealt with during the entire project is the instability of the Fe_2O_3 photo-anodes. One of the advantages with Fe_2O_3 in general is its stability, and several stable long-time measurements have been reported [10, 11]. The unstable photo-anodes complicate characteristic measurements, which for instance can be seen in the measurement with the addition of H_2O_2 in the electrolyte. The voltammetry results obtained in the ordinary electrolyte show lower current densities and higher onset potentials compared to the first measurements done on the same electrodes. It is, of course, not optimal to compare electrodes that for some unknown reason not perform as they should. The basic properties of these uniform Fe_2O_3 photo-anodes should be analysed in order to be able to fabricate reproducible electrodes that give the same result and are stable in time. This may, however, be difficult if the Fe deposition takes place in an evaporator that also handles other elements that may dope the Fe_2O_3 .

7.1 Outlook

Although no actual calculation was done on the total solar-to-hydrogen conversion efficiency, these thin Fe_2O_3 +overlayer photo-anodes are far from the benchmark efficiency of 10%. However, the purpose with project was not to achieve as high solar-

to-hydrogen efficiency as possible, but to analyse the effect of overlayers on Fe_2O_3 . A future project could be to deposit these overlayers on a nanostructured Fe_2O_3 sample with a much higher surface to volume ratio. Other characterisation methods could be utilised to study the ultrathin overlayers and their composition, for instance X-ray photoelectron spectroscopy for composition measurements, and transmission electron microscopy for imaging the overlayers and measure their thickness.

In conclusion, hydrogen generation via water splitting is a promising field which has made great progress the last decades. The step to large-scale commercial use may seem far away, but there is a lot left to learn and develop. I think and hope that the future is waiting for the breakthrough in this field, so that I in 50 years can look back at this thesis with a smile and realise what great progresses that have been made.

Bibliography

- [1] Daniel V. Schroeder. *An introduction to thermal physics*. Addison Wesley, San Francisco, 2000.
- [2] IEA. Key world energy statistics 2016. 2016. Available from: <https://www.iea.org/publications/freepublications/publication/key-world-energy-statistics.html>.
- [3] T Bak, J Nowotny, M Rekas, and C.C Sorrell. Photo-electrochemical hydrogen generation from water using solar energy. materials-related aspects. *International Journal of Hydrogen Energy*, 27(10):991 – 1022, 2002.
- [4] Enerdata. Global energy trends - 2016 edition. 2016. Available from: <https://www.enerdata.net/publications/reports-presentations/peak-energy-demand-co2-emissions-2016-world-energy.html>.
- [5] Takashi Hisatomi, Jun Kubota, and Kazunari Domen. Recent advances in semiconductors for photocatalytic and photoelectrochemical water splitting. *Chem. Soc. Rev.*, 43:7520–7535, 2014.
- [6] Akira Fujishima and Kenichi Honda. Electrochemical photolysis of water at a semiconductor electrode. *Nature*, 238(5358):37–38, 1972.
- [7] Andebet G. Tamirat, John Rick, Amare A. Dubale, Wei-Nien Su, and Bing-Joe Hwang. Using hematite for photoelectrochemical water splitting: a review of current progress and challenges. *Nanoscale Horiz*, 1(4):243–267, 2016.
- [8] Oscar Khaselev and John A. Turner. A monolithic photovoltaic-photoelectrochemical device for hydrogen production via water splitting. *Science*, 280(5362):425–427, 1998.
- [9] Jieyang Jia, Linsey C. Seitz, Jesse D. Benck, Yijie Huo, Yusi Chen, Jia Wei Desmond Ng, Taner Bilir, James S. Harris, and Thomas F. Jaramillo. Solar water splitting by photovoltaic-electrolysis with a solar-to-hydrogen efficiency over 30. *Nature Communications*, 7, 2016.
- [10] Jae Young Kim, Duck Hyun Youn, Kyoungwoong Kang, and Jae Sung Lee. Highly conformal deposition of an ultrathin FeOOH layer on a hematite nanostructure for efficient solar water splitting. *Angewandte Chemie International Edition*, 55(36):10854–10858, 2016.
- [11] Yufei Yuan, Jiuwang Gu, Kai-Hang Ye, Zhisheng Chai, Xiang Yu, Xiaobo Chen, Chuanxi Zhao, Yuanming Zhang, and Wenjie Mai. Combining bulk/surface engineering of hematite to synergistically improve its photoelectrochemical water splitting performance. *ACS Applied Materials & Interfaces*, 8(25):16071–16077, 2016. PMID: 27275649.
- [12] Jonathon Moir, Navid Soheilnia, Kristine Liao, Paul O’Brien, Yao Tian, Kenneth S. Burch, and Geoffrey A. Ozin. Activation of ultrathin films of hematite

- for photoelectrochemical water splitting via h₂ treatment. *ChemSusChem*, 8(9):1557–1567, 2015.
- [13] Philip H. Rieger, SpringerLink (Online service), and SpringerLink Archive (e-book collection). *Electrochemistry*. Springer Netherlands, Dordrecht, second edition, 1994.
- [14] Carl Nordling and Jonny Österman. *Physics handbook for science and engineering*. Studentlitteratur, Lund, 8., [rev.] edition, 2006.
- [15] Kittel, Charles and Paul McEuen. *Introduction to solid state physics*. Wiley, Hoboken, N.J, 8. edition, 2005.
- [16] Adrian W. Bott. Electrochemistry of semiconductors. *Current Separations*, 17(3):87–91, 1998.
- [17] Craig A Grimes, Oomman K Varghese, and Sudhir Ranjan. *Light, Water, Hydrogen - The Solar Generation of Hydrogen by Water Photoelectrolysis*. Springer US, 2008.
- [18] Roel van de Krol. *Principles of Photoelectrochemical Cells*, pages 13–67. Springer US, Boston, MA, 2012.
- [19] B. Gilbert, C. Frandsen, E. R. Maxey, and D. M. Sherman. Band-gap measurements of bulk and nanoscale hematite by soft x-ray spectroscopy. *Phys. Rev. B*, 79:035108, Jan 2009.
- [20] Li Fu, Hongmei Yu, Yongkun Li, Changkun Zhang, Xunying Wang, Zhigang Shao, and Baolian Yi. Ethylene glycol adjusted nanorod hematite film for active photoelectrochemical water splitting. *Phys. Chem. Chem. Phys.*, 16:4284–4290, 2014.
- [21] Yichuan Ling, Gongming Wang, Damon A. Wheeler, Jin Z. Zhang, and Yat Li. Sn-doped hematite nanostructures for photoelectrochemical water splitting. *Nano Letters*, 11(5):2119–2125, 2011. PMID: 21476581.
- [22] Susanta K. Mohapatra, Shiny E. John, Subarna Banerjee, and Mano Misra. Water photooxidation by smooth and ultrathin -fe₂o₃ nanotube arrays. *Chemistry of Materials*, 21(14):3048–3055, 2009.
- [23] Yongcai Qiu, Siu-Fung Leung, Qianpeng Zhang, Bo Hua, Qingfeng Lin, Zhanhua Wei, Kwong-Hoi Tsui, Yuegang Zhang, Shihe Yang, and Zhiyong Fan. Efficient photoelectrochemical water splitting with ultrathin films of hematite on three-dimensional nanophotonic structures. *Nano Letters*, 14(4):2123–2129, 2014. PMID: 24601797.
- [24] Andebet Gedamu Tamirat, Wei-Nien Su, Amare Aregahegn Dubale, Hung-Ming Chen, and Bing-Joe Hwang. Photoelectrochemical water splitting at low applied potential using a niOOH coated codoped (sn, zr) [small alpha]-fe₂o₃ photoanode. *J. Mater. Chem. A*, 3:5949–5961, 2015.
- [25] Benjamin Klahr, Sixto Gimenez, Francisco Fabregat-Santiago, Thomas Hamann, and Juan Bisquert. Water oxidation at hematite photoelectrodes: The role of surface states. *Journal of the American Chemical Society*, 134(9):4294–4302, 2012. PMID: 22303953.
- [26] Rui Liu, Zhi Zheng, Joshua Spurgeon, and Xiaogang Yang. Enhanced photoelectrochemical water-splitting performance of semiconductors by surface passivation layers. *Energy Environ. Sci.*, 7:2504–2517, 2014.

-
- [27] Chun Du, Xiaogang Yang, Matthew T. Mayer, Henry Hoyt, Jin Xie, Gregory McMahon, Gregory Bischooping, and Dunwei Wang. Hematite-based water splitting with low turn-on voltages. *Angewandte Chemie International Edition*, 52(48):12692–12695, 2013.
- [28] Zhebo Chen, Huyen N Dinh, and Eric Miller. *Photoelectrochemical Water Splitting - Standards, Experimental Methods, and Protocols*. Springer New York, 2013.
- [29] Beniamino Iandolo, Björn Wickman, Elin Svensson, Daniel Paulsson, and Anders Hellman. Tailoring charge recombination in photoelectrodes using oxide nanostructures. *Nano Letters*, 16(4):2381–2386, 2016. PMID: 26978576.
- [30] Anders Hellman, Beniamino Iandolo, Björn Wickman, Henrik Grönbeck, and Jonas Baltrusaitis. Electro-oxidation of water on hematite: Effects of surface termination and oxygen vacancies investigated by first-principles. *Surface Science*, 640:45 – 49, 2015. Reactivity Concepts at Surfaces: Coupling Theory with Experiment.
- [31] C. Riordan and R. Hulstrom. 'what is an air mass 1.5 spectrum?' *Conference Record of the IEEE Photovoltaic Specialists Conference*, 2:1085–1088, 1990.
- [32] Beniamino Iandolo, Bjorn Wickman, Brian Seger, Ib Chorkendorff, Igor Zoric, and Anders Hellman. Faradaic efficiency of o₂ evolution on metal nanoparticle sensitized hematite photoanodes. *Phys. Chem. Chem. Phys.*, 16:1271–1275, 2014.
- [33] Beniamino Iandolo, Haixiang Zhang, Bjorn Wickman, Igor Zoric, Gavin Conibeer, and Anders Hellman. Correlating flat band and onset potentials for solar water splitting on model hematite photoanodes. *RSC Adv.*, 5:61021–61030, 2015.
- [34] Derek J Gardiner and Pierre R Graves. *Practical Raman Spectroscopy*. Springer Berlin Heidelberg, 1989.
- [35] Peter C. Rieke, Brian D. Marsh, Laurie L Wood, Barbara J. Tarasevich, Jun Liu, Lin Song, and Glen E. Fryxell. Aqueous solution deposition kinetics of iron oxyhydroxide on sulfonic acid terminated self-assembled monolayers. *Langmuir*, 11(1):318–326, 1995.
- [36] D. L. A. de Faria, S. Venâncio Silva, and M. T. de Oliveira. Raman microspectroscopy of some iron oxides and oxyhydroxides. *Journal of Raman Spectroscopy*, 28(11):873–878, 1997.
- [37] C. Johnston and P. R. Graves. In situ raman spectroscopy study of the nickel oxyhydroxide electrode (noe) system. *Appl. Spectrosc.*, 44(1):105–115, Jan 1990.